

Searching for Singularities in Navier-Stokes Flows Based on the Ladyzhenskaya-Prodi-Serrin Conditions

Di Kang¹ and Bartosz Protas^{1,*}

¹ Department of Mathematics and Statistics, McMaster University
Hamilton, ON, Canada
January 15, 2022

Abstract

In this investigation we perform a systematic computational search for potential singularities in 3D Navier-Stokes flows based on the Ladyzhenskaya-Prodi-Serrin conditions. They assert that if the quantity $\int_0^T \|\mathbf{u}(t)\|_{L^q(\Omega)}^p dt$, where $2/p + 3/q \leq 1$, $q > 3$, is bounded, then the solution $\mathbf{u}(t)$ of the Navier-Stokes system is smooth on the interval $[0, T]$. In other words, if a singularity should occur at some time $t \in [0, T]$, then this quantity must be unbounded. We have probed this condition by studying a family of variational PDE optimization problems where initial conditions \mathbf{u}_0 are sought to maximize $\int_0^T \|\mathbf{u}(t)\|_{L^4(\Omega)}^8 dt$ for different T subject to suitable constraints. These problems are solved numerically using a large-scale adjoint-based gradient approach. Even in the flows corresponding to the optimal initial conditions determined in this way no evidence has been found for singularity formation, which would be manifested by unbounded growth of $\|\mathbf{u}(t)\|_{L^4(\Omega)}$. However, the maximum enstrophy attained in these extreme flows scales in proportion to $\mathcal{E}_0^{3/2}$, the same as found by Kang et al. (2020) when maximizing the finite-time growth of enstrophy. In addition, we also consider sharpness of an a priori estimate on the time evolution of $\|\mathbf{u}(t)\|_{L^4(\Omega)}$ by solving another PDE optimization problem and demonstrate that the upper bound in this estimate could be improved.

1 Introduction

This investigation concerns a systematic search for potentially singular behavior in three-dimensional (3D) Navier-Stokes flows. By formation of a “singularity” we mean the situation when an initially smooth solution no longer satisfies the governing equation in the classical (pointwise) sense. This so-called “blow-up problem” is one of the key open questions in mathematical fluid mechanics and, in fact, its importance for mathematics in general has been recognized by the Clay Mathematics Institute as one of its “millennium problems” [22]. Should such singular behavior indeed be possible in the solutions of the 3D Navier-Stokes problem, it would invalidate this system as a model of realistic fluid flows. Questions concerning global-in-time existence of smooth solutions remain open also for a number of other flow models including the 3D Euler equations [26] and some of the “active scalar” equations [40].

We consider the incompressible Navier-Stokes system defined on the 3D unit cube $\Omega = [0, 1]^3$ with periodic boundary conditions

$$\partial_t \mathbf{u} + \mathbf{u} \cdot \nabla \mathbf{u} + \nabla p - \nu \Delta \mathbf{u} = 0 \quad \text{in } \Omega \times (0, T], \quad (1a)$$

$$\nabla \cdot \mathbf{u} = 0 \quad \text{in } \Omega \times [0, T], \quad (1b)$$

$$\mathbf{u}(0) = \mathbf{u}_0, \quad (1c)$$

*Corresponding Author, Email: bprotas@mcmaster.ca

where the vector $\mathbf{u} = [u_1, u_2, u_3]^T$ is the velocity field, p is the pressure, $\nu > 0$ is the coefficient of kinematic viscosity and \mathbf{u}_0 is the initial condition. The velocity gradient $\nabla \mathbf{u}$ is a tensor with components $[\nabla \mathbf{u}]_{ij} = \partial_j u_i$, $i, j = 1, 2, 3$. The fluid density ρ is assumed constant and equal to unity ($\rho = 1$).

In our study an important role will be played by Lebesgue norms of the velocity field

$$\|\mathbf{u}(t)\|_{L^q(\Omega)} := \left(\int_{\Omega} |\mathbf{u}(t, \mathbf{x})|^q d\mathbf{x} \right)^{\frac{1}{q}}, \quad q \geq 1, \quad (2)$$

where “:=” means “equal to by definition”, such that the kinetic energy can be expressed as

$$\mathcal{K}(\mathbf{u}(t)) := \frac{1}{2} \|\mathbf{u}(t)\|_{L^2(\Omega)}^2. \quad (3)$$

Another important quantity is the enstrophy¹

$$\mathcal{E}(\mathbf{u}(t)) := \frac{1}{2} \int_{\Omega} |\nabla \times \mathbf{u}(t, \mathbf{x})|^2 d\mathbf{x} \quad (4)$$

and the two quantities are related via the energy equation

$$\frac{d\mathcal{K}(\mathbf{u}(t))}{dt} = -\nu \mathcal{E}(\mathbf{u}(t)). \quad (5)$$

While global in time existence of classical solutions of the Navier-Stokes system (1) remains an open question, it is known that suitably defined weak solutions, which need not satisfy the Navier-Stokes system pointwise in space and time, but rather in a certain integral sense only, exist globally in time [43]. An important tool in the study of the global-in-time regularity of classical (smooth) solutions are the so-called “conditional regularity results” stating additional conditions which must be satisfied by a weak solution in order for it to also be a smooth solution, i.e., to satisfy the Navier-Stokes system in the classical sense as well. One of the best known results of this type [23] is based on the enstrophy of the time-dependent velocity field $\mathbf{u}(t)$ and asserts that if the uniform bound

$$\sup_{0 \leq t \leq T} \mathcal{E}(\mathbf{u}(t)) < \infty \quad (6)$$

holds, then the regularity and uniqueness of the solution $\mathbf{u}(t)$ are guaranteed up to time T (to be precise, the solution remains in a certain Gevrey class).

In the light of condition (6) it is important to characterize the largest growth of enstrophy possible in Navier-Stokes flows. Using (1) its rate of growth can be expressed as $\frac{d\mathcal{E}(\mathbf{u}(t))}{dt} = -\nu \int_{\Omega} |\Delta \mathbf{u}|^2 d\mathbf{x} + \int_{\Omega} \mathbf{u} \cdot \nabla \mathbf{u} \cdot \Delta \mathbf{u} d\mathbf{x} =: \mathcal{R}(\mathbf{u}(t))$ which is subject to the following bound [45, 18]

$$\frac{d\mathcal{E}}{dt} \leq \frac{27}{8\pi^4 \nu^3} \mathcal{E}^3. \quad (7)$$

¹We note that unlike energy, cf. (3), enstrophy is often defined without the factor of 1/2. However, for consistency with earlier studies belonging to this research program [4, 5, 6, 7, 70, 35], we choose to retain this factor here.

By simply integrating the differential inequality in (7) with respect to time we obtain the finite-time bound

$$\mathcal{E}(\mathbf{u}(t)) \leq \frac{\mathcal{E}_0}{\sqrt{1 - \frac{27}{4\pi^4\nu^3} \mathcal{E}_0^2 t}} \quad (8)$$

which clearly becomes infinite at time $t_0 = 4\pi^4\nu^3/(27\mathcal{E}_0^2)$. Thus, based on estimate (8), it is not possible to establish the boundedness of the enstrophy $\mathcal{E}(\mathbf{u}(t))$ required in condition (6) and hence also the regularity of solutions globally in time.

In addition to the enstrophy condition (6), another important conditional regularity result is given by the family of the Ladyzhenskaya-Prodi-Serrin conditions asserting that Navier-Stokes flows $\mathbf{u}(t)$ are smooth and satisfy system (1) in the classical sense provided that [41, 60, 66]

$$\mathbf{u} \in L^p([0, T]; L^q(\Omega)), \quad 2/p + 3/q = 1, \quad q > 3. \quad (9)$$

These conditions were recently generalized in [25] to include norms of the derivatives of the velocity field and to account for velocity-pressure correlations in [69]. As regards the limiting case with $q = 3$, the corresponding condition was established in [21]

$$\mathbf{u} \in L^\infty([0, T]; L^3(\Omega)) \quad (10)$$

and a related blow-up criterion was recently obtained in [68].

Condition (9) implies that should a singularity form in a classical solution $\mathbf{u}(t)$ of the Navier-Stokes system (1) at some finite time $0 < t_0 < \infty$, then necessarily

$$\lim_{t \rightarrow t_0} \int_0^t \|\mathbf{u}(\tau)\|_{L^q(\Omega)}^p d\tau \rightarrow \infty, \quad 2/p + 3/q = 1, \quad q > 3. \quad (11)$$

At the same time, the time evolution of the solution norm $\|\mathbf{u}(t)\|_{L^q(\Omega)}$ on the time interval $[0, T]$ is subject to the some a priori bounds valid also for Leray-Hopf weak solutions [25] which might involve singularities. Such an estimate was discussed in [17]

$$\int_0^T \|\mathbf{u}(\tau)\|_{L^q(\Omega)}^{\frac{4q}{3(q-2)}} d\tau \leq C \mathcal{K}_0^{\frac{2q}{3(q-2)}}, \quad 2 \leq q \leq 6, \quad (12)$$

where $\mathcal{K}_0 := \mathcal{K}(\mathbf{u}_0)$ and $C > 0$ is a generic constant whose numerical value may vary between different estimates (since in [17] this estimate is stated without an explicit upper bound on the right-hand side (RHS), i.e., simply asserting the finiteness of the expression on the left-hand side (LHS), estimate (12) is derived in Appendix A). We note that the integral expressions in (11) and (12) differ in the exponent in the integrand which is smaller by a factor of 2 in the latter case. A related estimate, known already to Leray [43], concerns bounds on the rate of growth of the L^q norm and has the form [28, 65, 64]

$$\frac{1}{q} \frac{d}{dt} \|\mathbf{u}(t)\|_{L^q(\Omega)}^q \leq C \|\mathbf{u}(t)\|_{L^q(\Omega)}^{\frac{q(q-1)}{q-3}}, \quad q > 3. \quad (13)$$

This estimate, which is analogous to (7), makes it possible to obtain lower bounds on L^q norms of solutions undergoing a hypothetical singularity formation in finite time.

We add that in the context of the inviscid Euler system a conditional regularity result similar to (6) and (9)–(10) is given by the Beale-Kato-Majda (BKM) criterion [9]. Recently,

finite-time singularity formation in 3D axisymmetric Euler flows on domains exterior to a boundary with conical shape was proved in [20].

While the blow-up problem is fundamentally a question in mathematical analysis, a lot of computational studies have been carried out since the mid-'80s in order to shed light on the hydrodynamic mechanisms which might lead to singularity formation in finite time. Given that such flows evolving near the edge of regularity involve formation of very small flow structures, these computations typically require the use of state-of-the-art computational resources available at a given time. The computational studies focused on the possibility of finite-time blow-up in the 3D Navier-Stokes and/or Euler system include [13, 63, 12, 36, 58, 15, 54, 53, 29, 26, 32, 57, 14, 56, 16], all of which considered problems defined on domains periodic in all three dimensions. The investigations [19, 38, 27, 37] focused on the time evolution of vorticity moments and compared it against bounds on these quantities obtained using rigorous analysis. Recent computations [39] considered a “trefoil” configuration meant to be defined on an unbounded domain (although the computational domain was always truncated to a finite periodic box). A simplified semi-analytic model of vortex reconnection was recently developed and analyzed based on the Biot-Savart law and asymptotic techniques [50, 51]. We also mention the studies [49] and [67], along with references found therein, in which various complexified forms of the Euler equation were investigated. The idea of this approach is that, since the solutions to complexified equations have singularities in the complex plane, singularity formation in the real-valued problem is manifested by the collapse of the complex-plane singularities onto the real axis. Overall, the outcome of these investigations is rather inconclusive: while for the Navier-Stokes system most of the recent computations do not offer support for finite-time blow-up, the evidence appears split in the case of the Euler system. In particular, the studies [14] and [57] hinted at the possibility of singularity formation in finite time. In this connection we also highlight the computational investigations [47, 48] in which blow-up was documented in axisymmetric Euler flows on a bounded (tubular) domain. Recently, numerical evidence for blow-up in solutions of the Navier-Stokes system in 3D axisymmetric geometry with a degenerate variable diffusion coefficient was provided in [33].

The related question of (non)uniqueness of solutions of the Navier-Stokes system was considered in [30] where the authors focused on self-similar axisymmetric solutions corresponding to initial data \mathbf{u}_0 with a singularity at the origin chosen such that \mathbf{u}_0 is self-similar and does not belong to the space $L^3(\mathbb{R}^3)$. Nonunique solutions which do not satisfy conditions (9)–(10) were then found numerically using the scale-invariance property to transform the Navier-Stokes system to a nonlinear boundary-value problem. The problem of nonunique solutions of 2D Euler equations corresponding to singular initial data was recently tackled in [3].

A common feature of most of the aforementioned investigations was that the initial data for the Navier-Stokes or Euler system was chosen in an ad-hoc manner, based on some heuristic, albeit well-justified, arguments. A new approach to the study of extreme, possibly singular, behavior in fluid flows was ushered by Lu & Doering who framed these questions in terms of suitable variational optimization problems. In [44, 45] they showed that estimate (7) is in fact sharp up to a numerical prefactor, in the sense that there exists a family of velocity fields $\tilde{\mathbf{u}}_{\mathcal{E}_0} \in H^2(\Omega)$ parameterized by their enstrophy \mathcal{E}_0 with the property that $\frac{d}{dt}\mathcal{E}(\tilde{\mathbf{u}}_{\mathcal{E}_0}) \sim \mathcal{E}_0^3$ as $\mathcal{E}_0 \rightarrow \infty$. However, while these vector fields, which have the form of two colliding vortex rings, saturate estimate (7) *instantaneously*, the Navier-Stokes flows using these optimal fields as the initial data feature rapid depletion of the rate of enstrophy growth for $t > 0$ such that

little enstrophy is produced before it starts to decrease [7] (for blow-up to occur, enstrophy must be amplified at a sustained rate $\frac{d\mathcal{E}}{dt} \sim \mathcal{E}^\alpha$, with $\alpha \in (2, 3]$ for a sufficiently long time [35]). A research program where the sharpness of various energy-type a priori estimates for one-dimensional (1D) Burgers and two-dimensional (2D) Navier-Stokes flows was probed using variational optimization formulations was pursued in [4, 5, 6, 7, 70, 8]. While these systems are known to be globally well-posed [42], questions about the sharpness of these estimates are quite pertinent since these estimates are obtained in a similar way to the key estimates (8), (11), (12) and (13).

The question whether enstrophy can become unbounded in finite time in Navier-Stokes flows was investigated in [35] by finding optimal initial data $\tilde{\mathbf{u}}_{0;\mathcal{E}_0,T}$ with fixed enstrophy \mathcal{E}_0 such that the enstrophy is maximized at time T . This was done by solving numerically a family of optimization problems

Problem 0 *Given $\mathcal{E}_0, T \in \mathbb{R}_+$, find*

$$\begin{aligned} \tilde{\mathbf{u}}_{0;\mathcal{E}_0,T} &= \arg \max_{\mathbf{u}_0 \in \mathcal{Q}_{\mathcal{E}_0}} \mathcal{E}(T), \quad \text{where} \\ \mathcal{Q}_{\mathcal{E}_0} &:= \{ \mathbf{u} \in H^1(\Omega) : \nabla \cdot \mathbf{u} = 0, \mathcal{E}(\mathbf{u}) = \mathcal{E}_0 \}, \end{aligned}$$

for a broad range of values of \mathcal{E}_0 and T . While no evidence was found for unbounded growth of enstrophy in such extreme Navier-Stokes flows, this study revealed the following approximate relation describing how the largest attained enstrophy scales with the initial enstrophy in the most extreme scenarios

$$\max_{T>0} \mathcal{E}(T) \approx 0.224 \mathcal{E}_0^{1.49}. \quad (14)$$

Interestingly, solution of an analogous maximization problem for 1D viscous Burgers equation obtained in [4] produced extreme flows which obey an essentially the same power-law relation as (14), but with a different prefactor.

The goal of the present study is twofold: first, we will search for initial data \mathbf{u}_0 which, subject to suitable constraints to be defined below, might lead to unbounded growth of the integral in (11) as $t \rightarrow t_0$, therefore signaling the emergence of a singularity at time t_0 ; second, we will probe the sharpness of the a priori estimate (12) in terms of the exponent of \mathcal{K}_0 . More precisely, in regard to the second goal, the objective is to verify whether the maximum of the quantity on the LHS in (12) achievable under the Navier-Stokes dynamics (1) saturates the upper bound on the RHS, in the sense of exhibiting the same scaling with the initial energy \mathcal{K}_0 , which would indicate that this estimate cannot be improved by reducing the exponent of \mathcal{K}_0 . To fix attention, we will consider these questions for one only value of the parameter q . Concerning the first question, we have found no evidence of unbounded growth required in (11) to signal finite-time blow-up. However, interestingly, the families of the Navier-Stokes flows maximizing the quantity $\int_0^T \|\mathbf{u}(\tau)\|_{L^4(\Omega)}^8 d\tau$ for different T and different values of the constraint were found to also follow a power-law relation with the same exponent as in (14) for the maximum growth of enstrophy. In regard to the second question, we concluded that estimate (12) is not sharp, although the degree to which the upper bound overestimates the growth of the expression on the LHS with \mathcal{K}_0 is reduced as $T \rightarrow \infty$.

The structure of the paper is as follows: optimization problems designed to probe the two questions mentioned above are stated in the next section; then, in Section 3 we introduce the computational approach employed to solve these optimization problems; our computational

results are presented in Section 4, whereas their discussion and conclusions are deferred to Section 5; some additional technical material is collected in two appendices.

2 Optimization Problem

In this section we formulate optimization problems designed to provide insights about the two questions stated in Introduction. For concreteness, hereafter we will consider relations (11) and (12) with fixed values of the indices $q = 4$ and $p = 8$. The reason for choosing these particular values of p and q is our desire to work with integer-valued indices, which will simplify numerical computations, while remaining “close” to the limiting critical case corresponding to $q = 3$, cf. (10) (since this last condition is not given in terms of an integral expression, it would need to be studied using methods different from the approach developed here). We assume that with the given initial data \mathbf{u}_0 the Navier-Stokes system (1) admits classical solutions on the time interval $[0, T]$ and define the quantities

$$\Phi_T(\mathbf{u}_0) := \frac{1}{T} \int_0^T \|\mathbf{u}(\tau)\|_{L^4(\Omega)}^8 d\tau, \quad (15a)$$

$$\Psi_T(\mathbf{u}_0) := \frac{1}{T} \int_0^T \|\mathbf{u}(\tau)\|_{L^4(\Omega)}^{8/3} d\tau, \quad (15b)$$

where $\mathbf{u}(t)$ is the solution of (1) with the initial condition \mathbf{u}_0 . These quantities correspond to the integral expressions in (11) and (12), except for the presence of the prefactor T^{-1} whose role is to offset the growth of the integrals which may occur for large T even in the absence of potentially singular events.

The idea for probing condition (11) is to formulate and solve an optimization problem in order to find initial data \mathbf{u}_0 maximizing $\Phi_T(\mathbf{u}_0)$ for some $T > 0$. However, for such an optimization problem to be well defined, suitable constraints must be imposed on \mathbf{u}_0 and a natural choice would be to require $\|\mathbf{u}_0\|_{L^4(\Omega)} = B$ for some sufficiently large $0 < B < \infty$ (the important question about the function space in which this optimization problem should be posed is addressed below). Then, if a hypothetical singularity is to occur at some time $t_0 > T$, $\max_{\|\mathbf{u}_0\|_{L^4(\Omega)}=B} \Phi_T(\mathbf{u}_0)$ must become unbounded as $T \rightarrow t_0$. Of course, a priori we do not know whether or not a singularity may form, let alone at what time t_0 , so condition (11) can be probed by maximizing $\Phi_T(\mathbf{u}_0)$ for increasing T at a given value of B , and then repeating the process for larger B . This approach is justified by upper bounds available on the largest time t_0 when singularity might occur [55].

From the computational point of view, PDE-constrained optimization problems are formulated most conveniently in a Hilbert space [62]. While there exist solution approaches applicable in the more general setting of Banach spaces, e.g., [61], they are significantly harder to use in practice. Given the form of our constraint, we will therefore formulate the optimization problems in the “largest” Sobolev space with Hilbert structure which is contained in $L^4(\Omega)$. From the Sobolev embedding theorem in dimension 3 [2], we deduce

$$H^s(\Omega) \hookrightarrow L^4(\Omega), \quad s \geq \frac{3}{4}, \quad (16)$$

where the Sobolev space $H^s(\Omega)$ is endowed with the norm $\|\mathbf{z}\|_{H^s(\Omega)} = \|\mathbf{z}\|_{L^2(\Omega)} + \ell^{2s} \|\mathbf{z}\|_{\dot{H}^s(\Omega)}$, $\forall \mathbf{z} \in H^s(\Omega)$, where $\|\mathbf{z}\|_{\dot{H}^s(\Omega)} = \|\Delta^{s/2} \mathbf{z}\|_{L^2(\Omega)}$ is a semi-norm and $0 < \ell < \infty$ is the Sobolev

parameter (while for different values of ℓ the norms $\|\mathbf{z}\|_{H^s(\Omega)}$ are equivalent, the choice of this parameter will play a role in numerical computations, cf. Section 4). The fractional Laplacian is defined in terms of the Fourier transform \mathcal{F} as $\Delta^{s/2} := \mathcal{F}^{-1}(|\mathbf{k}|^s \mathcal{F}\mathbf{z})$, $s \in \mathbb{R}$, where $\mathbf{k} \in \mathbb{Z}^3$ is the wavevector. Thus, the largest Hilbert-Sobolev space embedded in $L^4(\Omega)$ is the space $H^{3/4}(\Omega)$ and it will provide the functional setting for our optimization problems.

We therefore arrive at the following

Problem 1 *Given $B, T \in \mathbb{R}_+$ and the objective functional $\Phi_T(\mathbf{u}_0)$ from equation (15a), find*

$$\begin{aligned} \tilde{\mathbf{u}}_{0;B,T} &= \arg \max_{\mathbf{u}_0 \in \mathcal{L}_B} \Phi_T(\mathbf{u}_0), \quad \text{where} \\ \mathcal{L}_B &:= \left\{ \mathbf{u} \in H^{3/4}(\Omega) : \nabla \cdot \mathbf{u} = 0, \int_{\Omega} \mathbf{u}_0 \, d\mathbf{x} = \mathbf{0}, \|\mathbf{u}_0\|_{L^4(\Omega)} = B \right\}, \end{aligned}$$

where the second condition in the definition of the constraint manifold \mathcal{L}_B fixes the mean momentum since this quantity is conserved under the evolution governed by the Navier-Stokes system (1).

Embedding (16) implies that $\forall \mathbf{u} \in H^{3/4}(\Omega) \, \|\mathbf{u}\|_{L^4(\Omega)} \leq C \|\mathbf{u}\|_{H^{3/4}(\Omega)}$ and this allows us to re-express the constraint on the initial data \mathbf{u}_0 in terms of its $H^{3/4}$ norm, which is quadratic in \mathbf{u}_0 and therefore easier to enforce in computations. This leads us to

Problem 2 *Given $S, T \in \mathbb{R}_+$ and the objective functional $\Phi_T(\mathbf{u}_0)$ from equation (15a), find*

$$\begin{aligned} \tilde{\mathbf{u}}_{0;S,T} &= \arg \max_{\mathbf{u}_0 \in \mathcal{H}_S} \Phi_T(\mathbf{u}_0), \quad \text{where} \\ \mathcal{H}_S &:= \left\{ \mathbf{u} \in H^{3/4}(\Omega) : \nabla \cdot \mathbf{u} = 0, \int_{\Omega} \mathbf{u}_0 \, d\mathbf{x} = \mathbf{0}, \|\mathbf{u}_0\|_{\dot{H}^{3/4}(\Omega)} = S \right\}. \end{aligned}$$

We note that while Problem 2 is defined in the space $H^{3/4}(\Omega)$, the last condition defining the constraint manifold \mathcal{H}_S is expressed in terms of the seminorm $\|\cdot\|_{\dot{H}^{3/4}(\Omega)}$. This is done to ensure the constraint manifold has a similar structure to the manifold \mathcal{L}_B in Problem 1 and to the constraint manifold used in [35].

A potential deficiency of Problem 1 is that the constraint $\|\mathbf{u}_0\|_{L^4(\Omega)} = S > 0$ does not define a bounded set in the space $H^{3/4}(\Omega)$, in the sense that one can construct a sequence $\mathbf{z}_n \in H^{3/4}(\Omega)$, $n \in \mathbb{Z}$, such that $\forall n \, \|\mathbf{z}_n\|_{L^4(\Omega)} = S$ and $\lim_{n \rightarrow \infty} \|\mathbf{z}_n\|_{H^{3/4}(\Omega)} = \infty$. However, while theoretically possible, such behavior has not been observed in the computations reported in Section 4.

As regards the second question we want to answer, concerning the sharpness of estimate (12), given that the upper bound in this estimate is expressed in terms of the initial energy \mathcal{K}_0 , a natural form of the corresponding optimization problem is given by

Problem 3 *Given $\mathcal{K}_0, T \in \mathbb{R}_+$ and the objective functional $\Psi_T(\mathbf{u}_0)$ from equation (15b), find*

$$\begin{aligned} \tilde{\mathbf{u}}_{0;\mathcal{K}_0,T} &= \arg \max_{\mathbf{u}_0 \in \mathcal{G}_{\mathcal{K}_0}} \Psi_T(\mathbf{u}_0), \quad \text{where} \\ \mathcal{G}_{\mathcal{K}_0} &= \left\{ \mathbf{u} \in H^{3/4}(\Omega) : \nabla \cdot \mathbf{u} = 0, \int_{\Omega} \mathbf{u}_0 \, d\mathbf{x} = \mathbf{0}, \frac{1}{2} \|\mathbf{u}_0\|_{L^2(\Omega)}^2 = \mathcal{K}_0 \right\}, \end{aligned}$$

Our approach to solution of Problems 1, 2 and 3 is described next.

3 Computational Approach

In this section we describe our approach to solution of optimization problems 1, 2 and 3 for given values of B , S or \mathcal{K}_0 and T . We adopt an “optimize-then-discretize” approach [31] in which a gradient method is first formulated in the infinite-dimensional (continuous) setting and only then the resulting equations and expressions are discretized for the purpose of numerical solution. A similar approach was recently used to solve the problem of determining the maximum growth of enstrophy in [35] with the corresponding 1D problem addressed earlier in [4]. To make the present paper self-contained, we recall key elements of the solution approach from [35]. However, there are also some important differences resulting from the functional setting and the nature of the constraints in Problems 1, 2 and 3 which we highlight. We also mention the Riemannian aspects of the optimization problems [1]. In our presentation below we first focus on solving Problem 2 as it arguably has the simplest structure and then discuss the modifications required to solve Problems 1 and 3.

3.1 Discrete Gradient Flow

Problem 2 is Riemannian in the sense that the maximizer $\tilde{\mathbf{u}}_{0;S,T}$ must be contained on a constraint manifold \mathcal{H}_S [1]. In order to locally characterize this manifold, we construct the tangent space $\mathcal{T}_{\mathbf{z}}\mathcal{H}_S$ at some point $\mathbf{z} \in \mathcal{H}_S$. The fixed-norm constraints can be expressed in terms of the function $F_X : H^{3/4}(\Omega) \rightarrow \mathbb{R}_+$, $F_X := \|\mathbf{z}\|_X$, where $X = L^4(\Omega), \dot{H}^{3/4}(\Omega), L^2(\Omega)$ respectively in Problems 1, 2 and 3. Then, the subspace tangent to the manifold defined in the space $H^{3/4}(\Omega)$ by the relation $F_X(\mathbf{z}) = S$ is given by the condition $\forall \mathbf{z}' \in H^{3/4}(\Omega)$ $F'(\mathbf{z}; \mathbf{z}') = \langle \nabla F_X(\mathbf{z}), \mathbf{z}' \rangle_{H^{3/4}(\Omega)} = 0$ which also defines the element $\nabla F_X(\mathbf{z})$ orthogonal to the subspace. Thus, since in Problem 2 we have $F_X(\mathbf{z}) = F_{\dot{H}^{3/4}}(\mathbf{z}) := \|\mathbf{z}\|_{\dot{H}^{3/4}}$, the tangent space to the manifold \mathcal{H}_S is defined as

$$\mathcal{T}_{\mathbf{z}}\mathcal{H}_S := \left\{ \mathbf{v} \in H^{3/4}(\Omega) : \nabla \cdot \mathbf{v} = 0, \int_{\Omega} \mathbf{v} d\mathbf{x} = \mathbf{0}, \langle \nabla F_{\dot{H}^{3/4}}(\mathbf{z}), \mathbf{v} \rangle_{H^{3/4}(\Omega)} = 0 \right\}, \quad (17)$$

where $\langle \nabla F_{\dot{H}^{3/4}}(\mathbf{z}), \mathbf{z}' \rangle_{H^{3/4}(\Omega)} = \langle \mathbf{z}, \mathbf{z}' \rangle_{\dot{H}^{3/4}(\Omega)}, \quad \forall \mathbf{z}' \in H^{3/4}(\Omega)$

(we note that in general $\nabla F_{\dot{H}^{3/4}}(\mathbf{z}) \neq \mathbf{z}$ since the constraint is defined in terms of the semi-norm).

The maximizer $\tilde{\mathbf{u}}_{0;S,T}$ can then be found as $\tilde{\mathbf{u}}_{0;S,T} = \lim_{n \rightarrow \infty} \mathbf{u}_{0;S,T}^{(n)}$ using the following iterative procedure representing a discretization of a gradient flow projected on \mathcal{H}_S

$$\begin{aligned} \mathbf{u}_{0;S,T}^{(n+1)} &= \mathbb{R}_{\mathcal{H}_S} \left(\mathbf{u}_{0;S,T}^{(n)} + \tau_n \mathbb{P}_{\mathcal{T}_n} \nabla \Phi_T \left(\mathbf{u}_{0;S,T}^{(n)} \right) \right), \\ \mathbf{u}_{0;S,T}^{(1)} &= \mathbf{u}^0. \end{aligned} \quad (18)$$

Here $\mathbf{u}_{0;S,T}^{(n)}$ is an approximation of the maximizer obtained at the n -th iteration, \mathbf{u}^0 is the initial guess, $\mathbb{P}_{\mathcal{T}_n} : H^{3/4}(\Omega) \rightarrow \mathcal{T}_n := \mathcal{T}_{\mathbf{u}_{0;S,T}^{(n)}}\mathcal{H}_S$ is an operator representing projection onto the tangent subspace (17) at the n th iteration, τ_n is the length of the step whereas $\mathbb{R}_{\mathcal{H}_S} : \mathcal{T}_n \rightarrow \mathcal{H}_S$ is a retraction from the tangent space to the constraint manifold [1]. A key element of the iterative procedure (18) is the evaluation of the gradient $\nabla \Phi_T$ of the objective functional Φ_T , cf. (15a), representing its (infinite-dimensional) sensitivity to perturbations of the initial data

\mathbf{u}_0 in the governing system (1). We emphasize that it is essential for the gradient to possess the required regularity, namely, $\nabla \Phi_T(\mathbf{u}_0) \in H^{3/4}(\Omega)$.

The first step to determine the gradient $\nabla \Phi_T$ is to consider the Gâteaux (directional) differential $\Phi'_T(\mathbf{u}_0; \cdot) : H^{3/4}(\Omega) \rightarrow \mathbb{R}$ of the objective functional Φ_T defined as $\Phi'_T(\mathbf{u}_0; \mathbf{u}'_0) := \lim_{\epsilon \rightarrow 0} \epsilon^{-1} [\Phi_T(\mathbf{u}_0 + \epsilon \mathbf{u}'_0) - \Phi_T]$ for some arbitrary perturbation $\mathbf{u}'_0 \in H^{3/4}(\Omega)$. The gradient $\nabla \Phi_T$ can then be extracted from the Gâteaux differential $\Phi'_T(\mathbf{u}_0; \mathbf{u}'_0)$ recognizing that, when viewed as a function of its second argument, this differential is a bounded linear functional on the space $H^{3/4}(\Omega)$ and we can therefore invoke the Riesz representation theorem [46]

$$\Phi'_T(\mathbf{u}_0; \mathbf{u}'_0) = \left\langle \nabla^{L^2} \Phi_T, \mathbf{u}'_0 \right\rangle_{L^2(\Omega)} = \left\langle \nabla \Phi_T, \mathbf{u}'_0 \right\rangle_{H^{3/4}(\Omega)}, \quad (19)$$

where the gradient $\nabla \Phi_T$ is the Riesz representer in the function space $H^{3/4}(\Omega)$. In (19) we also formally defined the gradient $\nabla^{L^2} \Phi_T$ determined with respect to the L^2 topology as it will be useful in subsequent computations. Given the definition of the objective functional in (15a), its Gâteaux differential can be expressed as

$$\Phi'_T(\mathbf{u}_0; \mathbf{u}'_0) = \frac{8}{T} \int_0^T \left(\|\mathbf{u}(t)\|_{L^4(\Omega)}^4 \int_{\Omega} |\mathbf{u}(t, \mathbf{x})|^2 \mathbf{u}(t, \mathbf{x}) \cdot \mathbf{u}'(t, \mathbf{x}) d\mathbf{x} \right) dt, \quad (20)$$

where the perturbation field $\mathbf{u}' = \mathbf{u}'(t, \mathbf{x})$ is a solution of the Navier-Stokes system linearized around the trajectory corresponding to the initial data \mathbf{u}_0 [31], i.e.,

$$\mathcal{L} \begin{bmatrix} \mathbf{u}' \\ p' \end{bmatrix} := \begin{bmatrix} \partial_t \mathbf{u}' + \mathbf{u}' \cdot \nabla \mathbf{u} + \mathbf{u} \cdot \nabla \mathbf{u}' + \nabla p' - \nu \Delta \mathbf{u}' \\ \nabla \cdot \mathbf{u}' \end{bmatrix} = \begin{bmatrix} \mathbf{0} \\ 0 \end{bmatrix}, \quad (21a)$$

$$\mathbf{u}'(0) = \mathbf{u}'_0 \quad (21b)$$

which is subject to the periodic boundary conditions and where p' is the perturbation of the pressure.

We note that expression (20) for the Gâteaux differential is not yet consistent with the Riesz form (19), because the perturbation \mathbf{u}'_0 of the initial data does not appear in it explicitly as a factor, but is instead hidden as the initial condition in the linearized problem, cf. (21b). In order to transform (20) to the Riesz form, we introduce the *adjoint states* $\mathbf{u}^* : [0, T] \times \Omega \rightarrow \mathbb{R}^3$ and $p^* : [0, T] \times \Omega \rightarrow \mathbb{R}$, and the following duality-pairing relation

$$\begin{aligned} \left(\mathcal{L} \begin{bmatrix} \mathbf{u}' \\ p' \end{bmatrix}, \begin{bmatrix} \mathbf{u}^* \\ p^* \end{bmatrix} \right) &:= \int_0^T \int_{\Omega} \mathcal{L} \begin{bmatrix} \mathbf{u}' \\ p' \end{bmatrix} \cdot \begin{bmatrix} \mathbf{u}^* \\ p^* \end{bmatrix} d\mathbf{x} dt = \overbrace{\left(\begin{bmatrix} \mathbf{u}' \\ p' \end{bmatrix}, \mathcal{L}^* \begin{bmatrix} \mathbf{u}^* \\ p^* \end{bmatrix} \right)}^{\Phi'_T(\mathbf{u}_0; \mathbf{u}'_0)} + \\ &\quad \int_{\Omega} \mathbf{u}'(T, \mathbf{x}) \cdot \mathbf{u}^*(T, \mathbf{x}) d\mathbf{x} - \int_{\Omega} \mathbf{u}'(0, \mathbf{x}) \cdot \mathbf{u}^*(0, \mathbf{x}) d\mathbf{x} = 0, \end{aligned} \quad (22)$$

where “ \cdot ” in the first integrand expression denotes the Euclidean dot product evaluated at (t, \mathbf{x}) . Performing integration by parts with respect to both space and time then allows us to define the *adjoint system* as

$$\mathcal{L}^* \begin{bmatrix} \mathbf{u}^* \\ p^* \end{bmatrix} := \begin{bmatrix} -\partial_t \mathbf{u}^* - \left[\nabla \mathbf{u}^* + (\nabla \mathbf{u}^*)^T \right] \mathbf{u} - \nabla p^* - \nu \Delta \mathbf{u}^* \\ -\nabla \cdot \mathbf{u}^* \end{bmatrix} = \begin{bmatrix} \mathbf{f} \\ 0 \end{bmatrix}, \quad (23a)$$

$$\text{where } \mathbf{f}(t, \mathbf{x}) := \frac{8}{T} \|\mathbf{u}(t)\|_{L^4(\Omega)}^4 |\mathbf{u}(t, \mathbf{x})|^2 \mathbf{u}(t, \mathbf{x}), \quad \mathbf{x} \in \Omega, \quad t \in [0, T], \quad (23b)$$

$$\mathbf{u}^*(T) = \mathbf{0} \quad (23c)$$

which is also subject to the periodic boundary conditions. We note that in identity (22) all boundary terms resulting from integration by parts with respect to the space variable vanish due to the periodic boundary conditions. The term $\int_{\Omega} \mathbf{u}'(T, \mathbf{x}) \cdot \mathbf{u}^*(T, \mathbf{x}) d\mathbf{x}$ resulting from integration by parts with respect to time vanishes because of the homogeneous terminal condition (23c) such that with the judicious choice of the source term (23b) identity (22) implies

$$\Phi'_T(\mathbf{u}_0; \mathbf{u}'_0) = \int_{\Omega} \mathbf{u}'_0(\mathbf{x}) \cdot \mathbf{u}^*(0, \mathbf{x}) d\mathbf{x}. \quad (24)$$

Applying the first equality in Riesz relations (19) to (24) we obtain the L^2 gradient as

$$\nabla^{L^2} \Phi_T = \mathbf{u}^*(0). \quad (25)$$

Our Sobolev gradient $\nabla \Phi_T(\mathbf{u}_0)$ is defined in a fractional Sobolev space $H^{3/4}(\Omega)$. However, since system (1) is defined on a periodic domain Ω , such a gradient can be determined in a similar manner to the case of a Sobolev space with an integer differentiability index [62]. We thus proceed by identifying the Gâteaux differential in (24) with the $H^{3/4}$ inner product. Then, recognizing that the perturbations \mathbf{u}'_0 are arbitrary, we obtain the following fractional elliptic boundary-value problem

$$\left[\text{Id} - \ell^{3/2} \Delta^{3/4} \right] \nabla \Phi_T(\mathbf{u}_0) = \nabla^{L^2} \Phi_T(\mathbf{u}_0) \quad \text{in } \Omega \quad (26)$$

subject to the periodic boundary conditions, which must be solved to determine $\nabla \Phi_T$. System (26) is conveniently solved in the Fourier space where it takes the form

$$\left[1 + \ell^{3/2} |\mathbf{k}|^{3/2} \right] \left[\widehat{\nabla \Phi_T(\mathbf{u}_0)} \right]_{\mathbf{k}} = \left[\widehat{\nabla^{L^2} \Phi_T(\mathbf{u}_0)} \right]_{\mathbf{k}}, \quad \mathbf{k} \in \mathbb{Z}^3 \setminus \mathbf{0}, \quad (27a)$$

$$\left[\widehat{\nabla \Phi_T(\mathbf{u}_0)} \right]_{\mathbf{0}} = \mathbf{0}, \quad (27b)$$

in which $[\widehat{\mathbf{z}}]_{\mathbf{k}} \in \mathbb{C}^3$ denotes the Fourier coefficient of the vector field \mathbf{z} corresponding to the wavevector \mathbf{k} . We remark that (27b) ensures that the Sobolev gradient $\nabla \Phi_T(\mathbf{u}_0)$ satisfies the zero-mean condition in Problem 2 (including this condition in system (27) is equivalent to projecting the resulting gradient on the subspace defined by this condition).

The gradient fields $\nabla^{L^2} \Phi_T$ and $\nabla \Phi_T$ can be interpreted as infinite-dimensional sensitivities of the objective functional Φ_T , cf. (15a), with respect to perturbations of the initial data \mathbf{u}_0 . While these two gradients point towards the same local maximizer, they represent distinct “directions”, since they are defined with respect to different norms (L^2 vs. $H^{3/4}$). As shown by [62], extraction of gradients in spaces of smoother functions such as $H^{3/4}(\Omega)$ can be interpreted as low-pass filtering of the L^2 gradients with the parameter ℓ_1 acting as the cut-off length-scale. Although Sobolev gradients obtained with different $0 < \ell_1 < \infty$ are equivalent, in the precise sense of norm equivalence [10], in practice the value of ℓ_1 tends to have a significant effect on the rate of convergence of gradient iterations (18) [62] and the choice of its numerical value will be discussed in Section 3.4. We emphasize that, while the $H^{3/4}$ gradient is used exclusively in the actual computations, cf. (18), the L^2 gradient is computed first as an intermediate step.

Evaluation of the L^2 gradient at a given iteration via (25) requires solution of the Navier-Stokes system (1) followed by solution of the adjoint system (23). We note that this system is a linear problem with coefficients and the source term determined by the solution of the Navier-Stokes system obtained earlier during the iteration. The adjoint system (23) is a *terminal*

value problem, implying that it must be integrated *backwards* in time from $t = T$ to $t = 0$ (since the term with the time derivative has a negative sign, this problem is well posed). Once the L^2 gradient is determined using (25), the corresponding Sobolev $H^{3/4}$ gradient can be obtained by solving problem (26). We add that the thus computed Sobolev gradient satisfies the divergence-free condition by construction, i.e., $\nabla \cdot (\nabla \Phi_T) = 0$.

3.2 Projection, Retraction and Arc-Maximization

The projection operator $\mathbb{P}_{\mathcal{T}_n}$ appearing in (18) is defined as [46], cf. (17),

$$\forall_{\mathbf{z} \in H^{3/4}(\Omega)} \quad \mathbb{P}_{\mathcal{T}_n} \mathbf{z} := \mathbf{z} - \frac{\left\langle \mathbf{z}, \nabla F_{\dot{H}^{3/4}} \left(\mathbf{u}_{0;S,T}^{(n)} \right) \right\rangle_{H^{3/4}(\Omega)}}{\left\| \nabla F_{\dot{H}^{3/4}} \left(\mathbf{u}_{0;S,T}^{(n)} \right) \right\|_{H^{3/4}(\Omega)}} \nabla F_{\dot{H}^{3/4}} \left(\mathbf{u}_{0;S,T}^{(n)} \right). \quad (28)$$

As can be readily verified, it preserves both the divergence-free and zero-mean conditions. The projection defined in (28) can be applied with obvious modifications consisting in changes of the norm and the inner product to Problem 3, but not to Problem 1. Expression for the projection operator in Problem 1 will be discussed in Section 3.3.

The retraction operator is defined as the normalization [1]

$$\forall_{\mathbf{z} \in \mathcal{T}_n} \quad \mathbb{R}_{\mathcal{H}_S}(\mathbf{z}) := \frac{S}{\|\mathbf{z}\|_{\dot{H}^{3/4}(\Omega)}} \mathbf{z} \quad (29)$$

which clearly also preserves the divergence-free and zero-mean properties of the argument. The retraction defined in (29) can be applied with obvious adjustments to Problems 1 and 3. Projection of the gradient $\nabla \Phi_T(\mathbf{u}_0)$ onto the tangent subspace \mathcal{T}_n via (28) followed by retraction (29) to the constraint manifold \mathcal{H}_S are illustrated schematically in Figure 1.

The step size τ_n in algorithm (18) is computed by solving the problem

$$\tau_n = \operatorname{argmax}_{\tau > 0} \Phi_T \left(\mathbb{R}_{\mathcal{H}_S} \left(\mathbf{u}_{0;S,T}^{(n)} + \tau \mathbb{P}_{\mathcal{T}_n} \nabla \Phi_T \left(\mathbf{u}_{0;S,T}^{(n)} \right) \right) \right) \quad (30)$$

which is done using a suitable derivative-free approach, such as a variant of Brent's algorithm [52, 59]. Equation (30) can be interpreted as a modification of the standard line-search problem where maximization is performed following an arc (a geodesic in the limit of infinitesimal step sizes) lying on the constraint manifold \mathcal{H}_S , rather than along a straight line.

3.3 Projection on Tangent Subspace in Problem 1

In Problem 1 the constraint is defined in terms of the function $F_{L^4}(\mathbf{z}) := \|\mathbf{z}\|_{L^4(\Omega)}$, such that the subspace tangent to the manifold \mathcal{L}_B is given by the condition $\langle \nabla F_{L^4}(\mathbf{z}), \mathbf{z}' \rangle_{H^{3/4}(\Omega)} = 0$, $\forall \mathbf{z}' \in H^{3/4}(\Omega)$, where $\langle \nabla F_{L^4}(\mathbf{z}), \mathbf{z}' \rangle_{H^{3/4}(\Omega)} = \langle |\mathbf{z}|^2 \mathbf{z}, \mathbf{z}' \rangle_{\dot{H}^{3/4}(\Omega)}$. We note that given the nonlinearity of the term $|\mathbf{z}|^2 \mathbf{z}$, the element $\nabla F_{L^4}(\mathbf{z})$ does not in general satisfy the divergence-free and zero-mean conditions, even if they are satisfied by \mathbf{z} . Thus, projection (28) must be modified

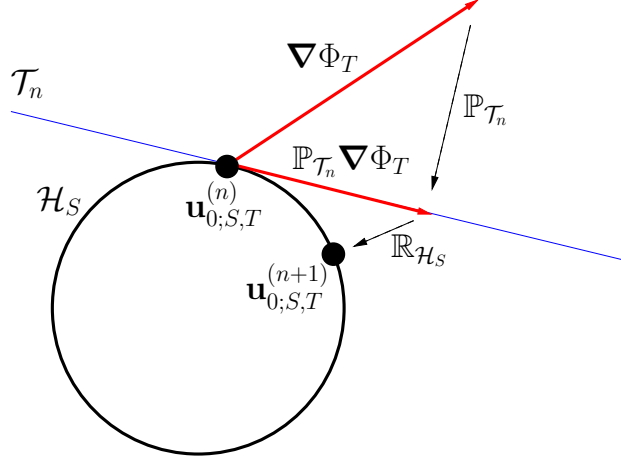


Figure 1: Schematic representation of projection (28) applied to the gradient $\nabla\Phi_T(\mathbf{u}_0)$ followed by retraction (29) to the manifold \mathcal{H}_S .

such that the result is both divergence-free and has zero mean which is done as follows

$$\forall \mathbf{z} \in H^{3/4}(\Omega) \quad \mathbb{P}_{\mathcal{T}_n} \mathbf{z} := \mathbf{z} - \frac{\left\langle \mathbf{z}, \nabla_{F_{L^4}} \left(\mathbf{u}_{0;B,T}^{(n)} \right) \right\rangle_{H^{3/4}(\Omega)}}{\left\langle \nabla_{F_{L^4}} \left(\mathbf{u}_{0;B,T}^{(n)} \right), \nabla_{F_{L^4}} \left(\mathbf{u}_{0;B,T}^{(n)} \right) \right\rangle_{H^{3/4}(\Omega)}} \overline{\nabla_{F_{L^4}} \left(\mathbf{u}_{0;B,T}^{(n)} \right)} \quad (31)$$

$$\text{where } \bar{\mathbf{v}} := \mathbf{v} - \nabla \Delta^{-1}(\nabla \cdot \mathbf{v}) - \int_{\Omega} \mathbf{v} d\mathbf{x}.$$

3.4 Numerical Implementation

The approach described in Sections 3.1–3.3 is implemented as described in detail in [35]. Here we summarize key elements of the numerical methodology and refer the reader to [35] for further particulars. Evaluation of the objective functionals (15a)–(15b) requires solution of the Navier-Stokes system (1) on the time interval $[0, T]$ with the given initial data \mathbf{u}_0 , whereas determination of the L^2 gradient (25) requires solution of the adjoint system (23). These two PDE systems are solved numerically with an approach combining a pseudo-spectral approximation of spatial derivatives with a fourth-order semi-implicit Runge-Kutta method [11] used to discretize these problems in time. In the evaluation of the nonlinear term in (1) and the terms with non-constant coefficients in (23) dealiasing is performed using the Gaussian filtering approach proposed in [34]. The velocity field $\mathbf{u} = \mathbf{u}(t, \mathbf{x})$ needed to evaluate the coefficients and the source term in the adjoint system (23) is saved at discrete time levels during solution of the Navier-Stokes system (1). In the definition of the Sobolev gradient in (26)–(27) we set $\ell = 2$ which was found by trial and error to maximize the rate of convergence of iterations (18). Massively parallel implementation based on MPI and using the `fftw` routines [24] to perform

Fourier transforms allowed us to employ resolutions varying from 128^3 to 512^3 in cases with low and high values of the constraints, respectively. In the latter cases solution of Problems 1, 2 and 3 for an intermediate length T of the time interval typically required a computational time of $\mathcal{O}(10^2)$ hours on $\mathcal{O}(10^2)$ CPU cores. The computational results presented in the next section have been thoroughly validated using strategies described in [35] to ensure they are converged with respect to refinement of the different numerical parameters.

Problems 1, 2 and 3 are non-convex and as such may admit multiple local maximizers. With the gradient-based approach (18), which relies on local common information only, we cannot assert whether the maxima we find are global or not. In order to find as many local maxima as possible, for each set of parameters T and B , S or \mathcal{K}_0 we solve Problems 1, 2 and 3 using different initial guesses \mathbf{u}^0 . For example, for Problem 1 we fix the value of the constraint B and then the corresponding branch of maximizing solutions is obtained by solving the problem for a sequence of (increasing or decreasing) values of T using the optimal solution $\tilde{\mathbf{u}}_{0,B,T}$ obtained for the previous value of T as the initial guess \mathbf{u}^0 . Then, another branch of maximizing solutions is obtained by repeating this process for a different value of the constraint B . We refer the reader to [35] for further details of this “continuation” approach. In addition, to make this search more exhausting, we have also used various random initial guesses and the optimal initial conditions found in [35] as the initial guess \mathbf{u}^0 .

4 Results

In this section we first discuss the results obtained by solving Problems 1 and 2 designed to search for initial data \mathbf{u}_0 that would trigger the appearance of a singularity in finite time. Next, we present the results obtained by solving Problem 3 defined to probe the sharpness of estimate (12). In these calculations we set $\nu = 0.01$ which is the same value as used in earlier studies of closely-related problems [45, 7, 35]. In addition to other diagnostic quantities, in our analysis of the different flows we will also consider their componentwise enstrophies $\mathcal{E}_i(\mathbf{u}(t))$, $i = 1, 2, 3$, associated with the three coordinate directions and defined as

$$\mathcal{E}_i(\mathbf{u}(t)) := \int_{\Omega} |(\nabla \times \mathbf{u}(t)) \cdot \mathbf{e}_i|^2 d\mathbf{x}, \quad i = 1, 2, 3, \quad (32)$$

where $\mathbf{e}_1, \mathbf{e}_2, \mathbf{e}_3$ are the unit vectors of the Cartesian coordinate system and we have the obvious identity $\forall t \quad \mathcal{E}(\mathbf{u}(t)) = \sum_{i=1}^3 \mathcal{E}_i(\mathbf{u}(t))$.

4.1 Flows Obtained as Solutions of Problems 1 and 2

Solution of Problems 1 and 2 has yielded two distinct maximizing branches in each case and representative solutions are shown in terms of the time evolution of the norm $\|\mathbf{u}(t)\|_{L^4(\Omega)}^4$ in Figures 2a and 2b, respectively. Both figures show evolutions obtained with the largest considered values of the constraints B and S for “short” and “long” optimization windows T . In regard to Problem 1, we see that for solutions from both maximizing branches the quantity $\|\mathbf{u}(t)\|_{L^4(\Omega)}^4$ exhibits a significant transient growth with larger maximum values $\max_{0 \leq t \leq T} \|\mathbf{u}(t)\|_{L^4(\Omega)}^4$ achieved for shorter optimization windows T . On the other hand, for Problem 2 we note that the norm $\|\mathbf{u}(t)\|_{L^4(\Omega)}^4$ exhibits monotone decrease with time for maximizing solutions from both branches, cf. Figure 2b. These flows are quite similar to each other in terms of the

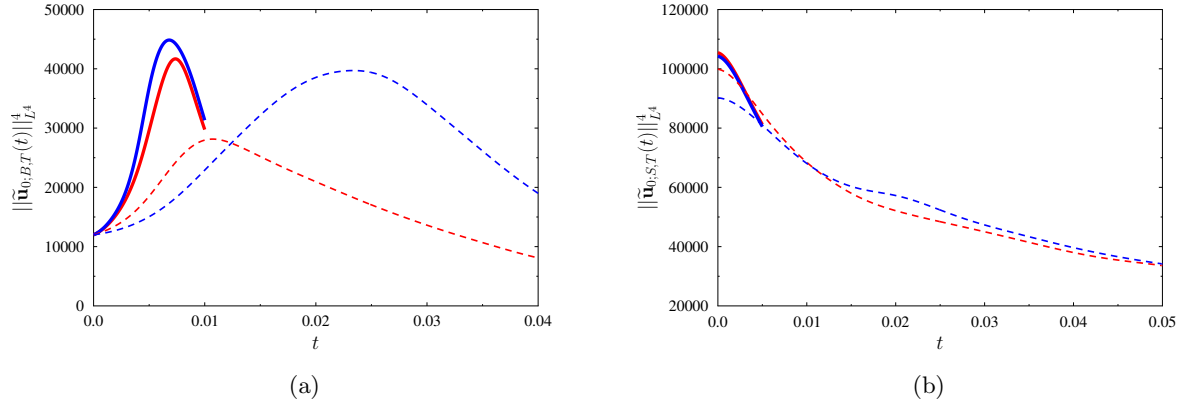


Figure 2: Time evolution of $\|\tilde{\mathbf{u}}(t)\|_{L^4}^4$ in the Navier-Stokes flows with optimal initial conditions obtained by solving (a) Problem 1 with $B^4 = 12,000$ and (b) Problem 2 with $S^2 = 2,000$ using two different lengths T of the optimization window (in each case the results are shown on the time interval $[0, T]$ where optimization was performed). In panel (a) the blue and red lines correspond to the partially symmetric and asymmetric branches, whereas in panel (b) they correspond to the symmetric and two-component branches.

evolution of the norm $\|\mathbf{u}(t)\|_{L^4(\Omega)}^4$ and, moreover, show weak dependence on the length T of the optimization window (in the sense that the flows obtained by solving Problem 2 with T_1 and T_2 such that $T_1 < T_2$ exhibit a similar evolution of $\|\mathbf{u}(t)\|_{L^4(\Omega)}^4$ for $t \in [0, T_1]$).

The maximizing branches obtained by solving Problems 1 and 2 with five different values of the constraints B and S are shown in terms of the dependence of the maximum values of the objective functional (15a) on the length T of the optimization window in Figures 3a and 3b, respectively. The presence of two distinct branches for each value of the constraint B and S is clearly evident, although the differences are small for solutions of Problem 2, cf. Figure 3b. We note that as regards solutions of Problem 1, for each value of the constraint B , the largest values of the objective functional $\Phi_T(\tilde{\mathbf{u}}_{0;B,T})$ are for both branches attained on optimization windows with length T decreasing with B , cf. Figure 3a. On the other hand, for solutions of Problem 2 obtained with a fixed value of the constraint S , the maxima of the objective functional $\Phi_T(\tilde{\mathbf{u}}_{0;S,T})$ are in all cases decreasing functions of the length T of the optimization window.

We now go on to discuss the structure of the extremal flows belonging to the different maximizing branches by characterizing their symmetry properties. We will do this by focusing on the componentwise enstrophies (32) whose time evolution in representative solutions of Problems 1 and 2 from both maximizing branches is shown in Figures 4a,b and 5a,b, respectively. As regards solutions of Problem 1 corresponding to the dominating branch which are shown in Figure 4a, we have $\mathcal{E}_1(\mathbf{u}(t)) = \mathcal{E}_2(\mathbf{u}(t)) > \mathcal{E}_3(\mathbf{u}(t))$, $\forall t \in [0, T]$, indicating that in these flows two vorticity components always contribute the same amount of enstrophy. On the other hand, for solutions corresponding to the second branch, the componentwise enstrophies $\mathcal{E}_1(\mathbf{u}(t))$, $\mathcal{E}_2(\mathbf{u}(t))$ and $\mathcal{E}_3(\mathbf{u}(t))$ remain distinct at almost all times $t \in [0, T]$. We will thus refer to these two

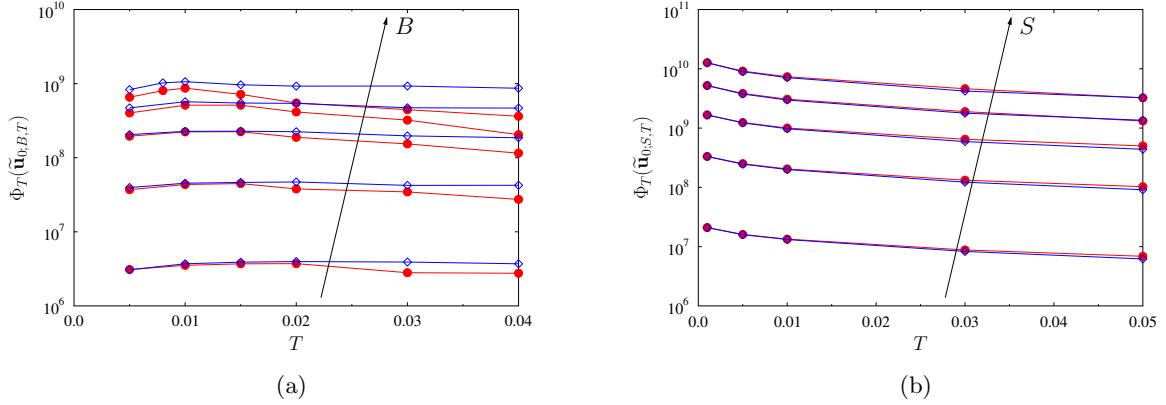


Figure 3: Dependence of the maxima of the objective functionals (a) $\Phi_T(\tilde{\mathbf{u}}_{0,B,T})$ from Problem 1 with $B^4 = 1,000, 3,000, 6,000, 9,000, 12,000$ and (b) $\Phi_T(\tilde{\mathbf{u}}_{0,S,T})$ from Problem 2 with $S^2 = 400, 800, 1,200, 1,600, 2,000$ on the length T of the optimization window. In panel (a) the blue and red lines correspond to the partially symmetric and asymmetric branches, whereas in panel (b) they correspond to the symmetric and two-component branches. Arrows indicate the directions of increase of the constraints B and S .

branches as “partially symmetric” and “asymmetric”. As concerns solutions of Problem 2, the results shown in Figures 5a and 5b indicate that we have $\mathcal{E}_1(\mathbf{u}(t)) = \mathcal{E}_2(\mathbf{u}(t)) = \mathcal{E}_3(\mathbf{u}(t))$ and $\mathcal{E}_1(\mathbf{u}(t)) = \mathcal{E}_2(\mathbf{u}(t)) > \mathcal{E}_3(\mathbf{u}(t)) = 0$, $\forall t \in [0, T]$, for the two branches, which we will henceforth refer to as “symmetric” and “two-component”, respectively. In solutions on these two branches the enstrophy is at all times equipartitioned between two and three vorticity components. We add that these symmetry properties characterizing different branches are robust and hold for different values of the parameters B , S and T .

In order to understand the physical structure of the extreme flows, the optimal initial conditions $\tilde{\mathbf{u}}_{0,B,T}$ and $\tilde{\mathbf{u}}_{0,S,T}$, obtained by solving Problems 1 and 2 are shown in Figures 6a,b and 7a,b. In both cases they were obtained with the largest considered values of the constraints, i.e., $B^4 = 12,000$ and $S^2 = 2,000$. For Problem 1, the initial conditions shown were obtained with $T = 0.01$, which is the length of the time window for which the largest value of the objective functional $\Phi_T(\tilde{\mathbf{u}}_{0,B,T})$ was attained, cf. Figure 3a. The initial condition corresponding to the dominating partially-symmetric branch has the form of two nearly parallel curved vortex sheets, cf. Figure 6a. On the other hand, the initial condition corresponding to the asymmetric branch has the form of a single curved vortex sheet, cf. Figure 6b. The time evolutions of the flows corresponding to the optimal initial conditions shown in Figures 6a and 6b are visualized in Movie 1 and Movie 2 available on-line. For Problem 2 with the shortest considered time window $T = 0.001$ which also produced the largest value of the objective functional $\Phi_T(\tilde{\mathbf{u}}_{0,S,T})$, cf. Figure 3b, in Figures 7a,b we see that the optimal initial condition $\tilde{\mathbf{u}}_{0,S,T}$ is very similar for both branches and has the form of a single vortex ring. The only difference is that the axis of the vortex ring is aligned with one of the coordinate directions in the case of the two-component branch and with the diagonal direction of the domain Ω

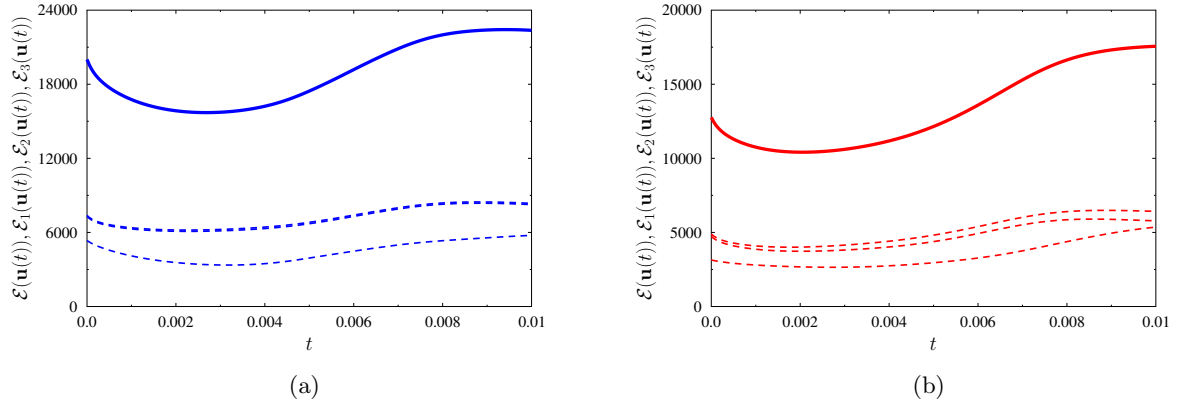


Figure 4: Evolution of (thick solid lines) the total entrophy $\mathcal{E}(\mathbf{u}(t))$ and (thin dashed lines) the componentwise entropies $\mathcal{E}_1(\mathbf{u}(t))$, $\mathcal{E}_2(\mathbf{u}(t))$, $\mathcal{E}_3(\mathbf{u}(t))$ in the solution of the Navier-Stokes system (1) with the optimal initial conditions $\tilde{\mathbf{u}}_{0;B,T}$ on (a) the partially symmetric branch and (b) the asymmetric branch obtained by solving Problem 1 with $B^4 = 12,000$ and $T = 0.01$.

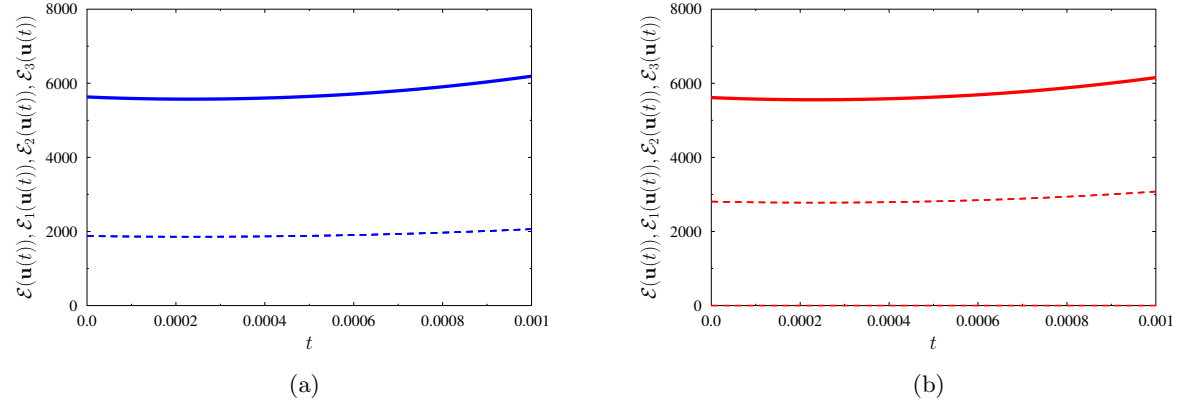


Figure 5: Evolution of (thick solid lines) the total entrophy $\mathcal{E}(\mathbf{u}(t))$ and (thin dashed lines) the componentwise entropies $\mathcal{E}_1(\mathbf{u}(t))$, $\mathcal{E}_2(\mathbf{u}(t))$, $\mathcal{E}_3(\mathbf{u}(t))$ in the solution of the Navier-Stokes system (1) with the optimal initial conditions $\tilde{\mathbf{u}}_{0;S,T}$ on (a) the symmetric branch and (b) the two-component branch obtained by solving Problem 2 with $S^2 = 2,000$ and $T = 0.001$.

for the symmetric branch. This property explains the equipartition of enstrophy observed in Figures 5a and 5b. As the value of the constraint S increases or the time window T shrinks, the corresponding optimal initial conditions $\tilde{\mathbf{u}}_{0,S,T}$ become more localized such that the orientation of the vortex structure with respect to the domain Ω plays a lesser role. This explains why the optimal initial data from the two branches obtained in Problem 2 yield very similar values of the objective function $\Phi_T(\tilde{\mathbf{u}}_{0,S,T})$, cf. Figure 3b. The time evolution of the flow corresponding to the optimal initial condition shown in Figures 7a is visualized in Movie 3 available on-line. We see that this evolution involves the translation and diffusion of the vortex ring.

We now return to the question whether the quantity in (11) with $q = 4$ can become unbounded in finite time, which would signal singularity formation. The results summarized in Figures 3a and 3b show no evidence of unbounded growth of the functional $\Phi_T(\mathbf{u}_0)$ when it is maximized by solving Problems 1 and 2. The maximum growth achieved by this functional is presented in Figures 8a and 8b where we plot $\max_T \Phi_T(\tilde{\mathbf{u}}_{0,B,T})$ and $\max_T \Phi_T(\tilde{\mathbf{u}}_{0,S,T})$, respectively, as functions of the constraints B and S . In other words, the maxima are taken over a maximizing branch with a fixed value of the constraint with respect to the length T of the optimization window. As is evident from Figures 8a and 8b, both $\max_T \Phi_T(\tilde{\mathbf{u}}_{0,B,T})$ and $\max_T \Phi_T(\tilde{\mathbf{u}}_{0,S,T})$ reveal clear power-law dependence on the values of the constraint which can be described by the following relations obtained by performing least-squares fits

$$\max_T \Phi_T(\tilde{\mathbf{u}}_{0,B,T}) \approx (0.6478 \pm 0.1153) \left(\|\tilde{\mathbf{u}}_{0,B,T}\|_{L^4(\Omega)}^4 \right)^{2.261 \pm 0.021}, \quad (33a)$$

$$\max_T \Phi_T(\tilde{\mathbf{u}}_{0,S,T}) \approx (9.308 \pm 0.373) \times 10^{-4} \left(\|\tilde{\mathbf{u}}_{0,S,T}\|_{H^{3/4}(\Omega)}^2 \right)^{3.979 \pm 0.005}. \quad (33b)$$

From Figure 3b we conclude that in Problem 2, the functional $\Phi_T(\tilde{\mathbf{u}}_{0,S,T})$ achieves its maximum with respect to T in the limit $T \rightarrow 0$, and thus $\max_T \Phi_T(\tilde{\mathbf{u}}_{0,S,T})$ depends only on the value of the constraint $\|\tilde{\mathbf{u}}_{0,S,T}\|_{L^4(\Omega)}$. Therefore, solving Problem 2 for $T \rightarrow 0$ is equivalent to seeking a divergence-free vector field with a fixed $H^{\frac{3}{4}}$ seminorm and a maximum L^4 norm, which explains the presence of an exponent close to 4 in (33b). As a result, the optimal initial data $\tilde{\mathbf{u}}_{0,S,T}$ obtained for different values of the constraint S with $T \rightarrow 0$ are identical up to normalization.

The results obtained for Problem 1 can also provide insights about the sharpness of the instantaneous estimate (13). More specifically, as shown in Appendix B, solutions of Problem 1 in the limit $T \rightarrow 0$ approximate solutions of the instantaneous optimization problem $\max_{\mathbf{u} \in \mathcal{L}_B} \frac{d}{dt} \|\mathbf{u}\|_{L^4(\Omega)}^4$, where $\frac{d}{dt} \|\mathbf{u}\|_{L^4(\Omega)}^4$ can be expressed using the Navier-Stokes system (1). Figure 9 shows the dependence of $\frac{d}{dt} \|\mathbf{u}(t)\|_{L^4(\Omega)}^4|_{t=0}$ approximated numerically based on the solution of the Navier-Stokes system (1) with the optimal initial condition $\tilde{\mathbf{u}}_{0,B,T}$ obtained from Problem 1 with the shortest considered optimization window $T = 0.001$ on $\|\tilde{\mathbf{u}}_{0,B,T}\|_{L^4(\Omega)}^4$. For both branches the figure reveals an essentially the same power-law relation

$$\frac{d}{dt} \|\mathbf{u}(t)\|_{L^4(\Omega)}^4|_{t=0} \approx (221.5 \pm 104) \left(\|\tilde{\mathbf{u}}_{0,B,T}\|_{L^4(\Omega)}^4 \right)^{1.117 \pm 0.05}. \quad (34)$$

It is clear that the exponent 1.117 in (34) is significantly smaller than the exponent of 3 predicted by estimate (13) with $q = 4$.

Finally, we compare the extreme flows analyzed above to the extreme flows constructed in [35] in terms of the relative growth of enstrophy. Dependence of the maximum attained enstrophy $\max_{t \geq 0} \mathcal{E}(t)$ on the initial enstrophy \mathcal{E}_0 in Navier-Stokes flows with the optimal

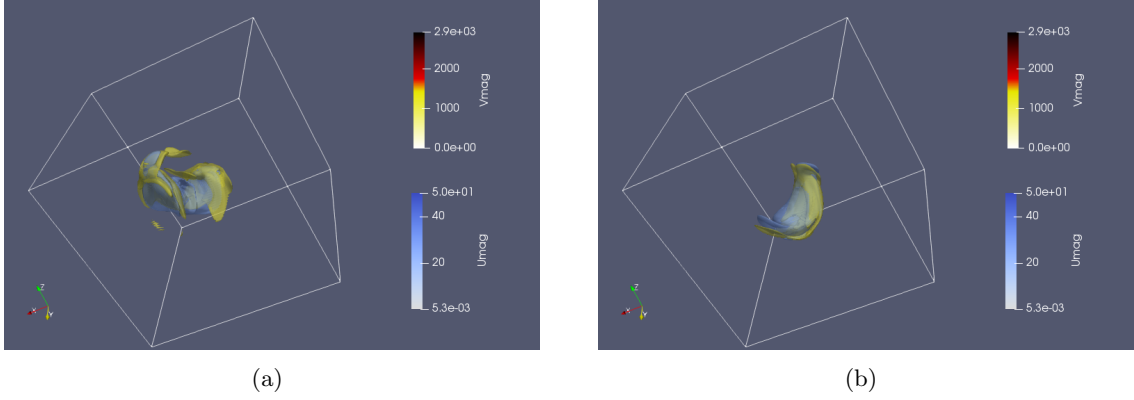


Figure 6: Optimal initial conditions $\tilde{\mathbf{u}}_{0;B,T}$ on (a) the partially symmetric branch and (b) asymmetric branch obtained by solving Problem 1 with $B^4 = 12,000$ and $T = 0.01$. Yellow and blue represent the iso-surfaces of the vorticity magnitude $|(\nabla \times \tilde{\mathbf{u}}_{0;B,T})(\mathbf{x})|$ and the velocity magnitude $|\tilde{\mathbf{u}}_{0;B,T}(\mathbf{x})|$, respectively. The time evolutions of the flows corresponding these initial conditions are visualized in Movie 1 and Movie 2 available as on-line.

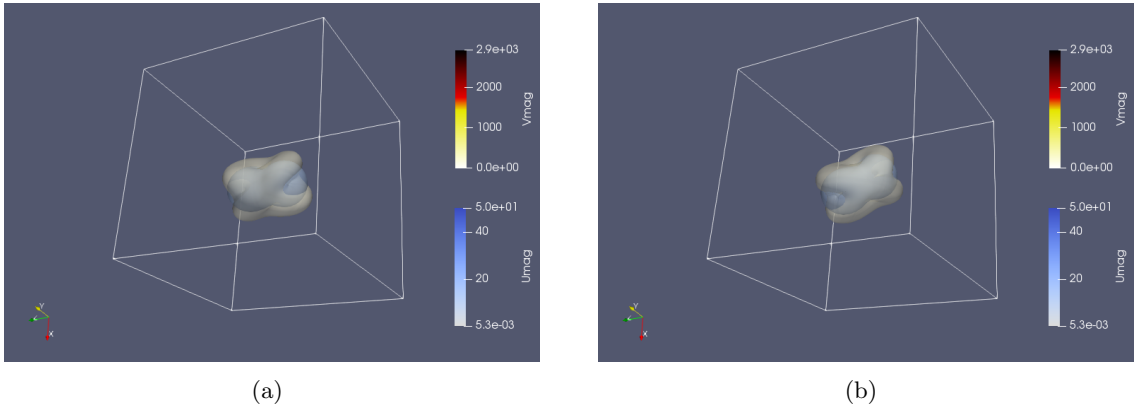


Figure 7: Optimal initial conditions $\tilde{\mathbf{u}}_{0;S,T}$ on (a) the two-component branch and (b) symmetric branch obtained by solving Problem 2 with $S^2 = 2,000$ and $T = 0.001$. Yellow and blue represent the iso-surfaces of the vorticity magnitude $|(\nabla \times \tilde{\mathbf{u}}_{0;S,T})(\mathbf{x})|$ and the velocity magnitude $|\tilde{\mathbf{u}}_{0;S,T}(\mathbf{x})|$, respectively. The time evolution of the flow corresponding the initial condition shown in (a) is visualized in Movie 3 available on-line.

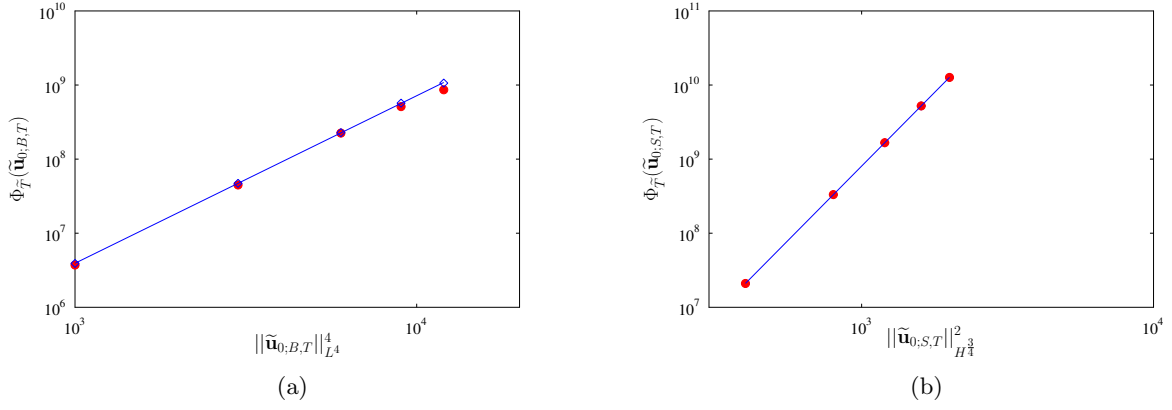


Figure 8: Dependence of (a) $\max_T \Phi_T(\tilde{\mathbf{u}}_{0;B,T})$ on $B^4 = \|\tilde{\mathbf{u}}_{0;B,T}\|_{L^4(\Omega)}^4$ and (b) $\max_T \Phi_T(\tilde{\mathbf{u}}_{0;S,T})$ on $S^2 = \|\tilde{\mathbf{u}}_{0;S,T}\|_{H^{3/4}(\Omega)}^2$ for Navier-Stokes flows with the optimal initial conditions $\tilde{\mathbf{u}}_{0;B,T}$ and $\tilde{\mathbf{u}}_{0;S,T}$ obtained by solving Problems 1 and 2, respectively. In panel (a) blue diamonds and red circles correspond to the partially symmetric and asymmetric branches, whereas in panel (b) these symbols correspond to the symmetric and two-component branches. Solid lines represent least-squares fits (33a) to the data from the partially symmetric branch in panel (a) and (33b) to the data from the symmetric branch in panel (b).

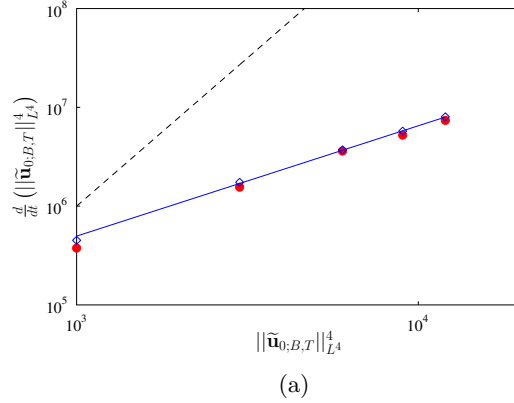


Figure 9: Dependence of the rate of change $\frac{d}{dt} \|\mathbf{u}(t)\|_{L^4(\Omega)}^4|_{t=0}$ on $\|\tilde{\mathbf{u}}_{0;B,T}\|_{L^4(\Omega)}^4$ for Navier-Stokes flows with the optimal initial conditions $\tilde{\mathbf{u}}_{0;B,T}$ obtained by solving Problems 1 with $T = 0.001$, which is the shortest considered time window. The blue diamonds and red circles correspond to the partially symmetric and asymmetric branches, respectively, whereas the blue solid line represents the least-squares fit (34). The dashed black line corresponds to the exponent of 3 obtained in (13) with $q = 4$.

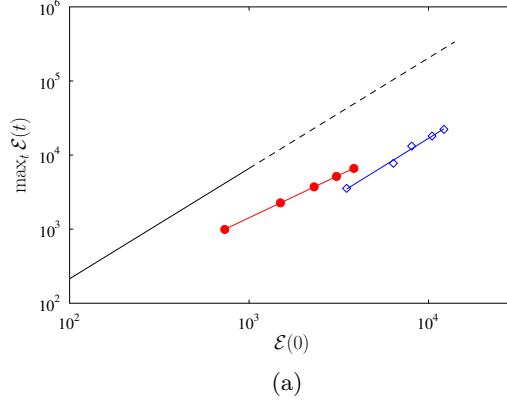


Figure 10: Dependence of the maximum attained enstrophy $\max_{t \geq 0} \mathcal{E}(t)$ on the initial enstrophy \mathcal{E}_0 in Navier-Stokes flows with the optimal initial conditions (blue diamonds) $\tilde{\mathbf{u}}_{0;B,T}$ obtained by solving Problems 1 (the partially-symmetric branch) and (red circles) $\tilde{\mathbf{u}}_{0;S,T}$ obtained by solving Problems 2 (the symmetric branch). Each symbol corresponds to a different value of the constraint B and S , and in all cases the results are presented for the length T of the optimization window producing the largest value of $\max_{t \geq 0} \mathcal{E}(t)$. The solid black line represents the relation $\max_{t \geq 0} \mathcal{E}(t) = C \mathcal{E}_0^{3/2}$ discovered in [35] and the dashed solid line its extrapolation to higher enstrophy values.

initial conditions $\tilde{\mathbf{u}}_{0;B,T}$ and $\tilde{\mathbf{u}}_{0;S,T}$ obtained by solving Problems 1 and 2 is shown in Figure 10, where, for comparison, we also show relation (14) discovered in [35]. The corresponding least-squares fits have the form

$$\max_{t \geq 0} \mathcal{E}(t) \approx (1.697 \pm 3.776) \times 10^{-2} \mathcal{E}_0^{1.499 \pm 0.249}, \quad (35a)$$

$$\max_{t \geq 0} \mathcal{E}(t) \approx (0.5155 \pm 0.0532) \mathcal{E}_0^{1.147 \pm 0.013}. \quad (35b)$$

It is intriguing to note that the power-law relation (35a) corresponding to the partially-symmetric branch obtained in Problem 1 features an essentially the same exponent close to $3/2$ as in (14), although the prefactor is much smaller.

4.2 Flows Obtained as Solutions of Problem 3

Solution of Problem 3 has yielded a single maximizing branch for each value of \mathcal{K}_0 with representative solutions shown in Figure 11 in terms of the time evolution of the norm $\|\mathbf{u}(t)\|_{L^4(\Omega)}^4$ for “short” and “long” optimization windows T . We see that, similarly to the solution of Problem 2 in Figure 2b, the norm $\|\mathbf{u}(t)\|_{L^4(\Omega)}^4$ is a decreasing function of time t . The maximizing branches obtained for different values of the constraint \mathcal{K}_0 are presented in terms of the dependence of the quantity $T\Psi_T(\tilde{\mathbf{u}}_{0;\mathcal{K}_0,T})$, which appears on the LHS of estimate (12), on T in Figure 12. We see that for each value of \mathcal{K}_0 the quantity $T\Psi_T(\tilde{\mathbf{u}}_{0;\mathcal{K}_0,T})$ is an increasing function of the length T of the optimization window approaching a certain limit as $T \rightarrow \infty$.

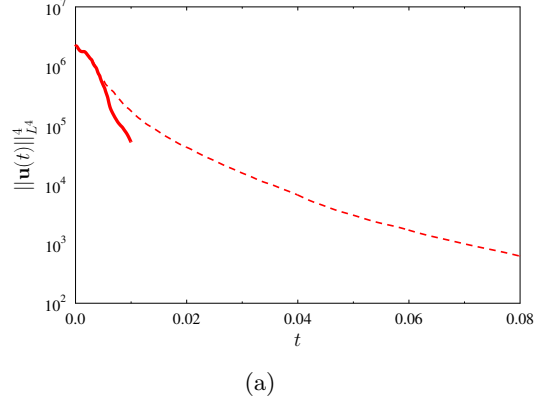


Figure 11: Time evolution of $\|\mathbf{u}(t)\|_{L^4}^4$ in the Navier-Stokes flows with optimal initial conditions $\tilde{\mathbf{u}}_{0;\mathcal{K}_0,T}$ obtained by solving Problem 3 with $\mathcal{K}_0 = 40$ using two different lengths $T = 0.01$ and $T = 0.08$ of the optimization window (in each case the results are shown on the time interval $[0, T]$ where optimization was performed).

In order to quantify its behavior in this limit, for each value of \mathcal{K}_0 we construct a fit to the dependence of $T\Psi_T(\tilde{\mathbf{u}}_{0;\mathcal{K}_0,T})$ on T in the form

$$g(T) := \psi_{\mathcal{K}_0} - \alpha e^{-\beta T}, \quad T > 0, \quad (36)$$

where $\psi_{\mathcal{K}_0}, \alpha, \beta \in \mathbb{R}^+$ are parameters determined via least-squares minimization, such that $\psi_{\mathcal{K}_0} \approx \lim_{T \rightarrow \infty} T\Psi_T(\tilde{\mathbf{u}}_{0;\mathcal{K}_0,T})$.

We now go on to discuss the structure of the extremal flows on the maximizing branches by characterizing their symmetry properties using the componentwise enstrophies (32). Their time evolution in representative solutions of Problem 3 is shown in Figures 13a,b for short and long optimization windows T . We note that for both time windows we have the property $\mathcal{E}_1(\mathbf{u}(t)) = \mathcal{E}_2(\mathbf{u}(t)) > \mathcal{E}_3(\mathbf{u}(t))$, $\forall t \in [0, T]$, the same as was observed for solutions of Problem 1 on the dominating branch, cf. Figure 4a. Hence, these optimal solutions can be described as partially symmetric. However, in contrast to solutions of Problem 1, the time evolution of the enstrophy in solutions of Problem 3 is much less regular and involves significantly higher values. This more “turbulent” nature of solutions of Problem 3 is also evident in the form of the corresponding optimal initial conditions $\tilde{\mathbf{u}}_{0;\mathcal{K}_0,T}$ shown for the two time windows in Figures 14a,b. As we can see, these optimal initial conditions are less regular and involve more small-scale features than the optimal initial condition obtained by solving Problem 1, cf. Figure 6a. The time evolution of the flow corresponding to the optimal initial condition shown in Figures 14a is visualized in Movie 4 available on-line. We see that this evolution involves the translation of a turbulent spot followed by its eventual bursting.

Next, we analyze estimate (12) in the limit of long optimization windows T where the term $\|\mathbf{u}(T)\|_{L^2(\Omega)}^2$, cf. (43a), becomes insignificant. To this end in Figure 15a we plot $\psi_{\mathcal{K}_0}$ from (36) as function of \mathcal{K}_0 and observe that

$$\psi_{\mathcal{K}_0} = \lim_{T \rightarrow \infty} T\Psi_T(\tilde{\mathbf{u}}_{0;\mathcal{K}_0,T}) \approx (3.17 \pm 0.9)\mathcal{K}_0^{0.998 \pm 0.082}, \quad (37)$$

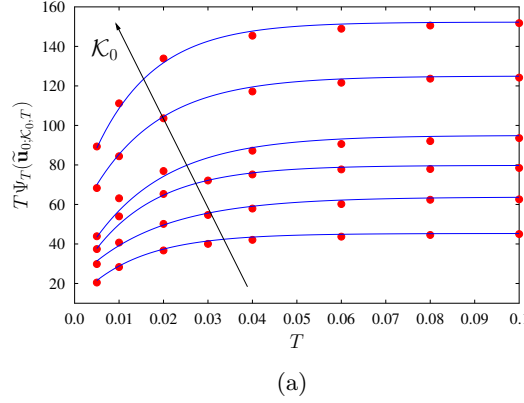


Figure 12: Dependence of the maxima of the quantity $T\Psi_T(\tilde{\mathbf{u}}_0; \kappa_0, T)$ on the length T of the optimization window. Red symbols represent solutions of Problem 3 for $\kappa_0 = 15, 20, 25, 30, 40, 50$ (arrow represents the direction of increase of κ_0) whereas blue lines are the fits obtained with formula (36).

which reveals a power-law dependence on κ_0 although the range of this quantity is not very extensive. The exponent is close to 1 which is smaller than the exponent $4/3$ predicted by estimate (12) with $q = 4$.

In order to obtain insights about the properties of estimate (12) for short and intermediate times T , we consider the relation

$$\Xi_{\kappa_0}(T) := \frac{\int_0^T \|\mathbf{u}(t)\|_{L^4}^{8/3} dt}{2\kappa_0 - \|\mathbf{u}(T)\|_{L^2(\Omega)}^2} \leq \frac{C}{2^{1/3}\nu} \kappa_0^{2/3} \quad (38)$$

obtained by dividing (43) by the expression in parentheses in (43b), such that the dependence on T is confined to the LHS. The quantity $\Xi_{\kappa_0}(T)$ is plotted as a function of κ_0 for different time windows T in Figure 15b. As we see in this figure, for a fixed κ_0 , $\Xi_{\kappa_0}(T)$ increases as T is reduced. In order to better understand the behavior of $\Xi_{\kappa_0}(T)$ for short optimization windows we consider the limit $T \rightarrow 0$ and define

$$\Theta_{\kappa_0} := \lim_{T \rightarrow 0} \Xi_{\kappa_0}(T) = \lim_{T \rightarrow 0} \frac{\Psi_T(\tilde{\mathbf{u}}_0; \kappa_0, T)}{2 \frac{\kappa_0 - \kappa(\mathbf{u}(T))}{T}} = \frac{\|\tilde{\mathbf{u}}_0; \varepsilon_0, T\|_{L^4(\Omega)}^{8/3}}{2\nu \mathcal{E}(\tilde{\mathbf{u}}_0; \varepsilon_0, T)} \quad (39)$$

where we used the energy equation (5). This quantity is also plotted in Figure 15b where we see that for each value of κ_0 we have $\Theta_{\kappa_0} > \Xi_{\kappa_0}(T)$, $T > 0$. Its dependence on κ_0 is approximated by the power-law relation

$$\Theta_{\kappa_0} \approx (4.963 \pm 0.492) \kappa_0^{0.32 \pm 0.03} \quad (40)$$

from which we deduce that the quantities Θ_{κ_0} and $\Xi_{\kappa_0}(T)$ exhibit a weaker growth with κ_0 than given by the expression on the RHS in (38) where the exponent is $2/3$. This thus demonstrates that estimate (12) is not sharp for any time window T .

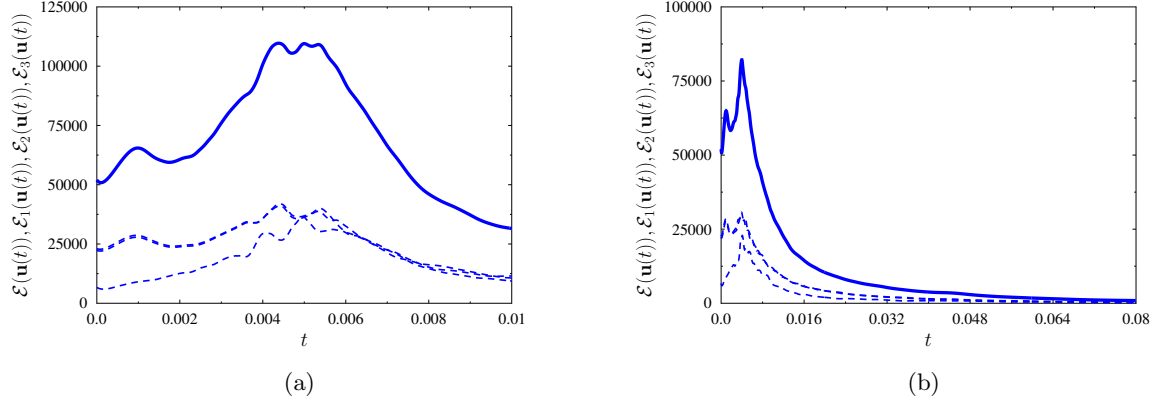


Figure 13: Evolution of (thick solid lines) the total entrophy $\mathcal{E}(\mathbf{u}(t))$ and (thin dashed lines) the componentwise entropies $\mathcal{E}_1(\mathbf{u}(t))$, $\mathcal{E}_2(\mathbf{u}(t))$, $\mathcal{E}_3(\mathbf{u}(t))$ in the solution of the Navier-Stokes system (1) with the optimal initial conditions $\tilde{\mathbf{u}}_{0;\mathcal{K}_0,T}$ obtained by solving Problem 3 with $\mathcal{K}_0 = 40$ and (a) $T = 0.01$ and (b) 0.08 .

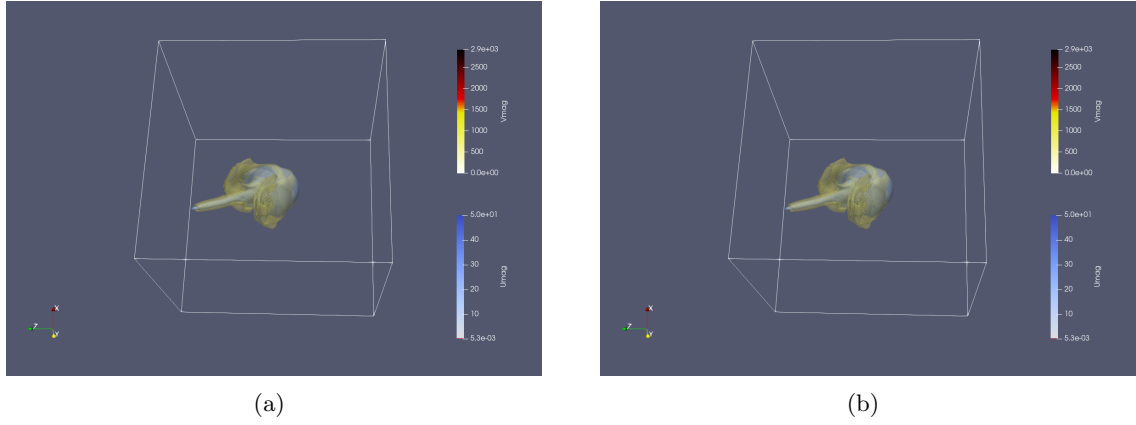


Figure 14: Optimal initial conditions $\tilde{\mathbf{u}}_{0;\mathcal{K}_0,T}$ obtained by solving Problem 3 with $\mathcal{K}_0 = 40$ and (a) $T = 0.01$ and (b) $T = 0.08$. Yellow and blue represent the iso-surfaces of the vorticity magnitude $|(\nabla \times \tilde{\mathbf{u}}_{0;\mathcal{K}_0,T})(\mathbf{x})|$ and the velocity magnitude $|\tilde{\mathbf{u}}_{0;\mathcal{K}_0,T}(\mathbf{x})|$, respectively. The time evolution of the flow corresponding the initial condition shown in (a) is visualized in Movie 4 available on-line.

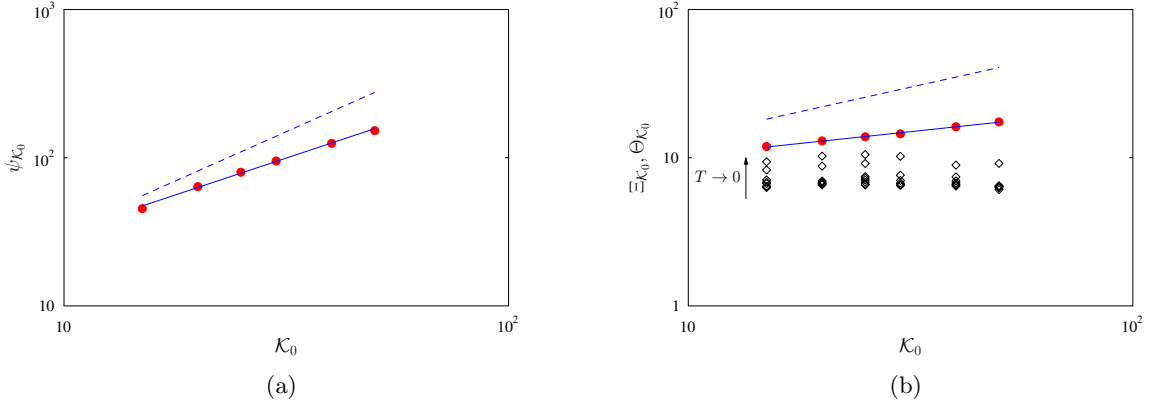


Figure 15: Dependence of (a) $\psi_{\mathcal{K}_0} \approx \lim_{T \rightarrow \infty} \Psi_T(\tilde{\mathbf{u}}_0; \mathcal{K}_0, T)$ and (b) (black diamonds) $\Xi_{\mathcal{K}_0}(T)$ and (red circles) $\Theta_{\mathcal{K}_0}$ on \mathcal{K}_0 for Navier-Stokes flows with the optimal initial conditions $\tilde{\mathbf{u}}_0; \mathcal{K}_0, T$ obtained by solving Problems 3. In (a) the dashed and solid lines represent, respectively, the expression on the RHS in estimate (12) (with $q = 4$ and an arbitrarily chosen constant C) and the least-squares fit (37). In (b) the dashed and solid lines represent, respectively, the expression on the RHS in (38) (with an arbitrarily chosen constant C) and the least-squares fit (40). The arrow indicates the trend with the decrease of T .

5 Discussion and Conclusions

In this study we have undertaken a systematic computational search for potential finite-time singularities in incompressible Navier-Stokes flows based on the Ladyzhenskaya-Prodi-Serrin conditional regularity criterion (9). This criterion asserts that a solution $\mathbf{u}(t)$ is smooth and satisfies the Navier-Stokes system (1) in the classical sense on the time interval $[0, T]$ provided the integral $\int_0^T \|\mathbf{u}(\tau)\|_{L^q(\Omega)}^{4q/(3(q-2))} d\tau$, where $q > 3$, is bounded. In our study we chose $q = 4$ and $p = 8$ which is the pair of integer-valued indices closest to the critical case with $p = 3$. To the best of our knowledge, this is the first such investigations based on the Ladyzhenskaya-Prodi-Serrin condition (9) and it complements earlier studies based on the enstrophy condition [45, 7, 35].

The idea of our approach is to consider classical solutions of the Navier-Stokes system (1) which might blow up in finite time. Initial data which might potentially lead to a singularity is sought by solving Problems 1 and 2 in which quantity (15a) is maximized subject to different sets of constraints. These problems were solved numerically with a state-of-the-art adjoint-based maximization approach formulated in the continuous (infinite-dimensional) setting. Since such approaches are most conveniently defined in Hilbert spaces, our optimal initial data was sought in the space $H^{3/4}(\Omega)$, which is the largest Sobolev space with Hilbert structure embedded in the space $L^4(\Omega)$ appearing in condition (9) when $q = 4$.

Problems 1 and 2 both admit two branches of maximizing solutions for a broad range of constraint values, cf. Figures 3a and 3b. It is interesting to note that while Problems 1 and 2 involve the same objective functional $\Phi_T(\mathbf{u}_0)$ maximized over the same function space $H^{3/4}(\Omega)$,

but subject to different, though related, constraints, their solutions are in fact very different. However, in none of the cases was there any evidence found for emergence of a singularity, in the sense that quantity (15a) remains bounded for all values of the constraints and all optimization windows T . However, when considering the corresponding growth of enstrophy, solutions of Problem 1 from the partially-symmetric branch were found to attain enstrophy values scaling in proportion to $\mathcal{E}_0^{3/2}$, cf. (35a). This is interesting because the same power-law dependence (but with a different, larger, prefactor) of the maximum attained enstrophy on \mathcal{E}_0 was obtained in Navier-Stokes flows with initial data constructed to maximize the finite-time growth of enstrophy in [35], cf. Figure 10, as well as in 1D Burgers flows with initial data determined in an analogous manner [4]. Thus, extreme Navier-Stokes flows with distinct structure obtained by maximizing two different quantities are characterized by the same power-law relation $\max_{t \geq 0} \mathcal{E}(t) \sim \mathcal{E}_0^{3/2}$ describing the dependence of the maximum attained enstrophy on the initial enstrophy. We recall that at present there are no rigorous a priori bounds on the growth of enstrophy and the best available estimate (8) has an upper bound which becomes infinite in finite time.

As the second main contribution of our study, we have considered the a priori estimate (12) and showed that it does not appear sharp, although the degree to which the expression on the RHS overestimates the growth of $\frac{1}{T} \int_0^T \|\mathbf{u}(\tau)\|_{L^4(\Omega)}^{8/3} d\tau$ with \mathcal{K}_0 is reduced as $T \rightarrow \infty$ (by “sharpness” we mean that the expression on the LHS in the estimate scales with \mathcal{K}_0 in the same way up to a prefactor as the upper bound on the RHS). This observation was deduced by solving Problem 3 for a range of values of \mathcal{K}_0 and T , and then extrapolating the results to large values of T . This lack of sharpness appears to be a consequence of the fact that the term $\|\mathbf{u}(T)\|_{L^2(\Omega)}^2$, which is dropped in (43a), is in general non-negligible for finite T , but becomes less significant as $T \rightarrow \infty$. These results thus demonstrate that estimate (12) may potentially be improved by reducing the power of \mathcal{K}_0 in the upper bound. This should not come as a surprise since the instantaneous estimate (13) was found not to be sharp as well, cf. Figure 9 and relation (34). We emphasize, however, that given the fact that Problems 1, 2 and 3 are non-convex, the observations made above cannot be regarded as definitive, since it is possible that despite our efforts we might not have found global maximizers.

As regards future studies, it is worthwhile to reconsider the problems investigated here using a formulation where the optimal initial data is sought directly in the space $L^4(\Omega)$ rather than in $H^{3/4}(\Omega)$. This can be done using an extension of the adjoint-based optimization approach we used to more general Banach spaces [61], which is however more technically involved. It is also interesting to probe the Ladyzhenskaya-Prodi-Serrin criterion (9) for a broad range of values of p and q , as well as to consider generalizations of this criterion involving derivatives of different order of the velocity field obtained in [25]. The limiting (critical) case with $q = 3$, cf. (10), is particularly interesting. However, given the non-differentiability of the norm $\|\cdot\|_{L^\infty([0,T])}$, this problem is not amenable to straightforward solution with the gradient-based optimization approach considered here. On the other hand, condition (10) can be probed by maximizing the finite-time growth of the norm $\|\mathbf{u}(T)\|_{L^3(\Omega)}$, in analogy to Problem 0 solved in [35]. Finally, it is also of interest to consider the problems studied here on the unbounded domain \mathbb{R}^3 instead of a torus.

Acknowledgments

This work is dedicated to the memory of the late Charlie Doering, our dear friend and collaborator, who inspired us to pursue this research direction. The authors wish to express thanks to John Gibbon, Evan Miller and Koji Ohkitani for enlightening and enjoyable discussions. They also acknowledge the support through an NSERC (Canada) Discovery Grant. Computational resources were provided by Compute Canada under its Resource Allocation Competition.

A Derivation of Estimate (12) with an Explicit Upper Bound

We begin with the Gagliardo–Nirenberg inequality

$$\|D^j \mathbf{u}\|_{L^p} \leq C \|D^m \mathbf{u}\|_{L^r}^\alpha \|\mathbf{u}\|_{L^q}^{1-\alpha}, \quad \text{where } \frac{1}{p} = \frac{j}{n} + \left(\frac{1}{r} - \frac{m}{n}\right) \alpha + \frac{1-\alpha}{q} \quad \text{and} \quad \frac{j}{m} \leq \alpha \leq 1. \quad (41)$$

Setting $j = 0$, $m = 1$, $r = 2$, $q = 2$, and $n = 3$ we obtain $\frac{1}{p} = 0 + \left(\frac{1}{2} - \frac{1}{3}\right) \alpha + \frac{1-\alpha}{2}$ and $\alpha = \frac{3(p-2)}{2p}$, such that for $2 \leq p \leq 6$ inequality (41) becomes

$$\|\mathbf{u}\|_{L^p} \leq C \|\nabla \mathbf{u}\|_{L^2}^\alpha \|\mathbf{u}\|_{L^2}^{1-\alpha}. \quad (42)$$

Raising both sides of (42) to the power $2/\alpha$, integrating with respect to time over $[0, T]$ and then using the energy equation (5) yields

$$\begin{aligned} \int_0^T \|\mathbf{u}(t)\|_{L^p}^{\frac{4p}{3(p-2)}} dt &\leq \int_0^T C \|\nabla \mathbf{u}(t)\|_{L^2}^2 \|\mathbf{u}(t)\|_{L^2}^{\frac{2(1-\alpha)}{\alpha}} dt \\ &\leq C (\|\mathbf{u}_0\|_{L^2})^{\frac{2(1-\alpha)}{\alpha}} \int_0^T \|\nabla \mathbf{u}(t)\|_{L^2}^2 dt \\ &= \frac{C}{2\nu} \|\mathbf{u}_0\|_{L^2}^{\frac{2(1-\alpha)}{\alpha}} (\|\mathbf{u}_0\|_{L^2}^2 - \|\mathbf{u}(T)\|_{L^2}^2) \end{aligned} \quad (43a)$$

$$\leq C \mathcal{K}_0^{\frac{2p}{3(p-2)}}, \quad 2 \leq p \leq 6. \quad (43b)$$

On the other hand, we can deduce from [25, Theorem 2(i)] that

$$\int_0^T \|\mathbf{u}(t)\|_{L^p}^{\frac{p}{p-3}} dt \leq C \left(\int_0^T \|\mathbf{u}(t)\|_{L^2}^2 dt \right)^{\frac{3}{2}} \leq C \mathcal{K}_0^3, \quad p > 6. \quad (44)$$

The ranges of validity of estimates (43) and (44) do not overlap, however, in the borderline case when $p = 6$ the expressions on the LHS in the two estimates coincide, yet the upper bound in the first estimate is $C \mathcal{K}_0$ and therefore has a smaller exponent than the upper bound in the second estimate.

B Problem 1 in the Limit $T \rightarrow 0$

In this Appendix we show that solutions of Problem 1 approximate solutions of the instantaneous optimization problem $\max_{\mathbf{u} \in \mathcal{L}_B} \frac{d}{dt} \|\mathbf{u}\|_{L^q(\Omega)}^q$, $q > 3$ in the limit $T \rightarrow 0$. We have for

$p, q \geq 1$

$$\begin{aligned}
\left. \frac{d\|\mathbf{u}(t)\|_{L^q(\Omega)}^p}{dt} \right|_{t=0} &= \frac{\|\mathbf{u}(T)\|_{L^q(\Omega)}^p - \|\mathbf{u}_0\|_{L^q(\Omega)}^p}{T} + \mathcal{O}(T) \\
&= \frac{\frac{d}{dT} \int_0^T \|\mathbf{u}(t)\|_{L^q(\Omega)}^p dt - \|\mathbf{u}_0\|_{L^q(\Omega)}^p}{T} + \mathcal{O}(T) \\
&= \frac{\frac{1}{T} \int_0^T \|\mathbf{u}(t)\|_{L^q(\Omega)}^p dt + \mathcal{O}(T) - \|\mathbf{u}_0\|_{L^q(\Omega)}^p}{T} + \mathcal{O}(T),
\end{aligned}$$

where we used the first-order finite-difference approximation of the derivative twice and the fundamental theorem of calculus. Then, after taking the maximum on both sides we obtain for $T \rightarrow 0$

$$\max_{\mathbf{u} \in \mathcal{L}_B} \left. \frac{d\|\mathbf{u}(t)\|_{L^q(\Omega)}^p}{dt} \right|_{t=0} = \frac{\frac{1}{T} \max_{\mathbf{u} \in \mathcal{L}_B} \int_0^T \|\mathbf{u}(t)\|_{L^q(\Omega)}^p dt - \|\mathbf{u}_0\|_{L^q(\Omega)}^p}{T} + \mathcal{O}(1). \quad (45)$$

Finally, to be able to relate this result to estimate (13), we apply the chain rule to obtain

$$\max_{\mathbf{u} \in \mathcal{L}_B} \left. \frac{d\|\mathbf{u}(t)\|_{L^q(\Omega)}^q}{dt} \right|_{t=0} = \frac{q}{p} \|\mathbf{u}_0\|_{L^q(\Omega)}^{q-p} \left(\frac{\frac{1}{T} \max_{\mathbf{u} \in \mathcal{L}_B} \int_0^T \|\mathbf{u}(t)\|_{L^q(\Omega)}^p dt - \|\mathbf{u}_0\|_{L^q(\Omega)}^p}{T} + \mathcal{O}(1) \right). \quad (46)$$

References

- [1] P.-A. Absil, R. Mahony, and R. Sepulchre. *Optimization Algorithms on Matrix Manifolds*. Princeton University Press, 2008.
- [2] R. A. Adams and J. F. Fournier. *Sobolev Spaces*. Elsevier, 2005.
- [3] Wen Shen Alberto Bressan. A posteriori error estimates for self-similar solutions to the Euler equations. *Discrete & Continuous Dynamical Systems*, 41(1):113–130, 2021.
- [4] D. Ayala and B. Protas. On maximum enstrophy growth in a hydrodynamic system. *Physica D*, 240:1553–1563, 2011.
- [5] D. Ayala and B. Protas. Maximum palinstrophy growth in 2D incompressible flows. *Journal of Fluid Mechanics*, 742:340–367, 2014.
- [6] D. Ayala and B. Protas. Vortices, maximum growth and the problem of finite-time singularity formation. *Fluid Dynamics Research*, 46(3):031404, 2014.
- [7] D. Ayala and B. Protas. Extreme vortex states and the growth of enstrophy in 3D incompressible flows. *Journal of Fluid Mechanics*, 818:772–806, 2017.
- [8] Diego Ayala, Charles R. Doering, and Thilo M. Simon. Maximum palinstrophy amplification in the two-dimensional Navier-Stokes equations. *Journal of Fluid Mechanics*, 837:839–857, 2018.

- [9] J. T. Beale, T. Kato, and A. Majda. Remarks on the breakdown of smooth solutions for the 3-D Euler equations. *Comm. Math. Phys.*, 94(1):61–66, 1984.
- [10] M. S. Berger. *Nonlinearity and Functional Analysis*. Academic Press, 1977.
- [11] T. R. Bewley. *Numerical Renaissance*. Renaissance Press, 2009.
- [12] M. E. Brachet. Direct simulation of three-dimensional turbulence in the Taylor-Green vortex. *Fluid Dynamics Research*, 8:1–8, 1991.
- [13] M. E. Brachet, D. I. Meiron, S. A. Orszag, B. G. Nickel, R. H. Morf, and U. Frisch. Small-scale structure of the Taylor-Green vortex. *Journal of Fluid Mechanics*, 130:411–452, 1983.
- [14] M. D. Bustamante and M. Brachet. Interplay between the Beale-Kato-Majda theorem and the analyticity-strip method to investigate numerically the incompressible Euler singularity problem. *Phys. Rev. E*, 86:066302, 2012.
- [15] M. D. Bustamante and R. M. Kerr. 3D Euler about a 2D symmetry plane. *Physica D*, 237:1912–1920, 2008.
- [16] Ciro S. Campolina and Alexei A. Mailybaev. Chaotic blowup in the 3d incompressible euler equations on a logarithmic lattice. *Phys. Rev. Lett.*, 121:064501, Aug 2018.
- [17] P. Constantin. Remarks on the Navier-Stokes equations. In L. Sirovich, editor, *New Perspectives in Turbulence*, pages 229–261. Springer, Berlin, 1991.
- [18] C. R. Doering. The 3D Navier-Stokes problem. *Annual Review of Fluid Mechanics*, 41:109–128, 2009.
- [19] Diego A. Donzis, John D. Gibbon, Anupam Gupta, Robert M. Kerr, Rahul Pandit, and Dario Vincenzi. Vorticity moments in four numerical simulations of the 3D Navier-Stokes equations. *Journal of Fluid Mechanics*, 732:316–331, 2013.
- [20] Tarek M. Elgindi and In-Jee Jeong. Finite-time Singularity formation for Strong Solutions to the axi-symmetric 3D Euler Equations. arXiv:1802.09936, 2018.
- [21] L Escauriaza, G A Seregin, and Vladimir Sverak. $L^{3,\infty}$ -solutions of the navier-stokes equations and backward uniqueness. *Russian Mathematical Surveys*, 58(2):211–250, apr 2003.
- [22] C. L. Fefferman. Existence and smoothness of the Navier-Stokes equation. available at <http://www.claymath.org/sites/default/files/navierstokes.pdf>, 2000. Clay Millennium Prize Problem Description.
- [23] C. Foias and R. Temam. Gevrey class regularity for the solutions of the Navier-Stokes equations. *Journal of Functional Analysis*, 87:359–369, 1989.
- [24] Matteo Frigo and Steven G. Johnson. *FFTW User’s Manual*. Massachusetts Institute of Technology, 2003.

- [25] J. D. Gibbon. Weak and Strong Solutions of the 3D Navier–Stokes Equations and Their Relation to a Chessboard of Convergent Inverse Length Scales. *Journal of Nonlinear Science*, Jul 2018. (published on-line).
- [26] J. D. Gibbon, M. Bustamante, and R. M. Kerr. The three–dimensional Euler equations: singular or non–singular? *Nonlinearity*, 21:123–129, 2008.
- [27] J.D Gibbon, D. Donzis, A. Gupta, R.M. Kerr, R. Pandit, and D. Vincenzi. Regimes of nonlinear depletion and regularity in the 3D Navier-Stokes equations. *Nonlinearity*, 27(1–19), 2014.
- [28] Y. Giga. Solutions for semilinear parabolic equations in L^p and regularity of weak solutions of the Navier-Stokes system. *Journal of Differential Equations*, 62(2):186–212, 1986.
- [29] T. Grafke, H. Homann, J. Dreher, and R. Grauer. Numerical simulations of possible finite-time singularities in the incompressible Euler equations: comparison of numerical methods. *Physica D*, 237:1932–1936, 2008.
- [30] J. Guilloid and V. Sverak. Numerical investigations of non-uniqueness for the Navier-Stokes initial value problem in borderline spaces. arXiv:1704.00560, 2017.
- [31] M. D. Gunzburger. *Perspectives in Flow Control and Optimization*. SIAM, 2003.
- [32] T. Y. Hou. Blow-up or no blow-up? a unified computational and analytic approach to 3D incompressible Euler and Navier–Stokes equations. *Acta Numerica*, pages 277–346, 2009.
- [33] T. Y. Hou and D. Huang. Potential Singularity Formation of 3D Axisymmetric Navier-Stokes Equations with Degenerate Diffusion Coefficients. arXiv:2102.06663, 2021.
- [34] T. Y. Hou and R. Li. Computing nearly singular solutions using pseudo-spectral methods. *Journal of Computational Physics*, 226:379–397, 2007.
- [35] Di Kang, Dongfang Yun, and Bartosz Protas. Maximum amplification of enstrophy in three-dimensional Navier-Stokes flows. *Journal of Fluid Mechanics*, 893:A22, 2020.
- [36] R. M. Kerr. Evidence for a singularity of the three-dimensional, incompressible Euler equations. *Phys. Fluids A*, 5:1725–1746, 1993.
- [37] R. M. Kerr. Bounds for Euler from vorticity moments and line divergence. *Journal of Fluid Mechanics*, 729:R2, 2013.
- [38] Robert M. Kerr. Swirling, turbulent vortex rings formed from a chain reaction of reconnection events. *Physics of Fluids*, 25:065101, 2013.
- [39] Robert M. Kerr. Enstrophy and circulation scaling for Navier-Stokes reconnection. *Journal of Fluid Mechanics*, 839:R2, 2018.
- [40] A. Kiselev. Regularity and blow up for active scalars. *Math. Model. Nat. Phenom.*, 5:225–255, 2010.

- [41] A. A. Kiselev and O. A. Ladyzhenskaya. On the existence and uniqueness of the solution of the nonstationary problem for a viscous, incompressible fluid. *Izv. Akad. Nauk SSSR Ser. Mat.*, 21(5):655–680, 1957.
- [42] H. Kreiss and J. Lorenz. *Initial-Boundary Value Problems and the Navier-Stokes Equations*, volume 47 of *Classics in Applied Mathematics*. SIAM, 2004.
- [43] Jean Leray. Sur le mouvement d’un liquide visqu’eux emplissant l’espace. *Acta Mathematica*, 63(1):193–248, 1934.
- [44] L. Lu. *Bounds on the enstrophy growth rate for solutions of the 3D Navier-Stokes equations*. PhD thesis, University of Michigan, 2006.
- [45] L. Lu and C. R. Doering. Limits on enstrophy growth for solutions of the three-dimensional Navier–Stokes equations. *Indiana University Mathematics Journal*, 57:2693–2727, 2008.
- [46] D. Luenberger. *Optimization by Vector Space Methods*. John Wiley and Sons, 1969.
- [47] G. Luo and T. Y. Hou. Potentially Singular Solutions of the 3D Axisymmetric Euler Equations. *Proceedings of the National Academy of Sciences*, 111(36):12968–12973, 2014.
- [48] G. Luo and T. Y. Hou. Toward the Finite-Time Blowup of the 3D Incompressible Euler Equations: a Numerical Investigation. *SIAM: Multiscale Modeling and Simulation*, 12(4):1722–1776, 2014.
- [49] T. Matsumoto, J. Bec, and U. Frisch. Complex-space singularities of 2D Euler flow in lagrangian coordinates. *Physica D*, 237:1951–1955, 2008.
- [50] H. K. Moffatt and Yoshifumi Kimura. Towards a finite-time singularity of the Navier-Stokes equations Part 1. Derivation and analysis of dynamical system. *Journal of Fluid Mechanics*, 861:930–967, 2019.
- [51] H. K. Moffatt and Yoshifumi Kimura. Towards a finite-time singularity of the Navier-Stokes equations. part 2. vortex reconnection and singularity evasion. *Journal of Fluid Mechanics*, 870:R1, 2019.
- [52] J. Nocedal and S. J. Wright. *Numerical Optimization*. Springer, 1999.
- [53] K. Ohkitani. A miscellany of basic issues on incompressible fluid equations. *Nonlinearity*, 21:255–271, 2008.
- [54] K. Ohkitani and P. Constantin. Numerical study of the Eulerian–Lagrangian analysis of the Navier-Stokes turbulence. *Phys. Fluids*, 20:1–11, 2008.
- [55] Koji Ohkitani. Late formation of singularities in solutions to the navier–stokes equations. *Journal of Physics A: Mathematical and Theoretical*, 49(1):015502, dec 2016.
- [56] P. Orlandi, S. Pirozzoli, M. Bernardini, and G. F. Carnevale. A minimal flow unit for the study of turbulence with passive scalars. *Journal of Turbulence*, 15:731–751, 2014.

- [57] P. Orlandi, S. Pirozzoli, and G. F. Carnevale. Vortex events in Euler and Navier-Stokes simulations with smooth initial conditions. *Journal of Fluid Mechanics*, 690:288–320, 2012.
- [58] R. B. Pelz. Symmetry and the hydrodynamic blow-up problem. *Journal of Fluid Mechanics*, 444:299–320, 2001.
- [59] W. H. Press, B. P. Flannery, S. A. Teukolsky, and W. T. Vetterling. *Numerical Recipes*. Cambridge University Press, 1986.
- [60] Giovanni Prodi. Un teorema di unicità per le equazioni di Navier-Stokes. *Annali di Matematica Pura ed Applicata*, 48(1):173–182, Dec 1959.
- [61] B. Protas. Adjoint-based optimization of PDE systems with alternative gradients. *Journal of Computational Physics*, 227:6490–6510, 2008.
- [62] B. Protas, T. Bewley, and G. Hagen. A comprehensive framework for the regularization of adjoint analysis in multiscale PDE systems. *Journal of Computational Physics*, 195:49–89, 2004.
- [63] A. Pumir and E. Siggia. Collapsing solutions to the 3D Euler equations. *Phys. Fluids A*, 2:220–241, 1990.
- [64] James C. Robinson and Witold Sadowski. A local smoothness criterion for solutions of the 3d navier-stokes equations. *Rendiconti del Seminario Matematico della Università di Padova*, 131:159–178, 2014.
- [65] James C. Robinson, Witold Sadowski, and Ricardo P. Silva. Lower bounds on blow up solutions of the three-dimensional navier stokes equations in homogeneous sobolev spaces. *Journal of Mathematical Physics*, 53(11):115618, 2012.
- [66] James Serrin. On the interior regularity of weak solutions of the Navier-Stokes equations. *Archive for Rational Mechanics and Analysis*, 9(1):187–195, Jan 1962.
- [67] M. Siegel and R. E. Caflisch. Calculation of complex singular solutions to the 3D incompressible Euler equations. *Physica D*, 238:2368–2379, 2009.
- [68] T. Tao. Quantitative bounds for critically bounded solutions to the Navier-Stokes equations. arXiv:1908.04958, 2020.
- [69] Chuong V. Tran, Xinwei Yu, and David G. Dritschel. Velocity pressure correlation in navier stokes flows and the problem of global regularity. *Journal of Fluid Mechanics*, 911:A18, 2021.
- [70] Dongfang Yun and Bartosz Protas. Maximum Rate of Growth of Enstrophy in Solutions of the Fractional Burgers Equation. *Journal of Nonlinear Science*, 28(1):395–422, Feb 2018.